Accepted for publication in ApJ
Preprint typeset using LaTeX style emulateapj v. 5/2/11

SPITZER SPECTROSCOPY OF INFRARED-LUMINOUS GALAXIES: DIAGNOSTICS OF AGN AND STAR FORMATION AND CONTRIBUTION TO TOTAL INFRARED LUMINOSITY

Heath V. Shipley[1], Casey Papovich[1], George H. Rieke[2], Arjun Dey[3], Buell T. Jannuzi[2,3], John Moustakas[4], Benjamin Weiner[2]

Accepted for publication in ApJ

ABSTRACT

We use mid-infrared (MIR) spectroscopy from the *Spitzer* Infrared Spectrograph (IRS) to study the nature of star-formation and supermassive black hole accretion for a sample of 65 IR-luminous galaxies at $0.02 < z < 0.6$ with $F(24\mu\mathrm{m}) > 1.2$ mJy. The MIR spectra cover wavelengths 5-38μm, spanning the polycyclic aromatic hydrocarbon (PAH) features and important atomic diagnostic lines. Our sample of galaxies corresponds to a range of total IR luminosity, $\mathrm{L_{IR}} = \mathrm{L(8\text{-}1000\mu m)} = 10^{10}\text{-}10^{12} L_{\odot}$ (median $\mathrm{L_{IR}}$ of $3.0\times10^{11}\mathrm{L_{\odot}}$). We divide our sample into a subsample of galaxies with *Spitzer* IRAC 3.6–8.0 μm colors indicative of warm dust heated by an AGN (IRAGN) and those galaxies whose colors indicate star-formation processes (non-IRAGN). Compared to the non-IRAGN, the IRAGN show smaller PAH emission equivalent widths, which we attribute to an increase in mid-IR continuum from the AGN. We find that in both the IRAGN and star-forming samples, the luminosity in the PAH features correlates strongly with [Ne II] $\lambda12.8\mu$m emission line, from which we conclude that the PAH luminosity directly traces the instantaneous star-formation rate (SFR) in both the IRAGN and star-forming galaxies. We compare the ratio of PAH luminosity to the total IR luminosity, and we show that for most IRAGN star-formation accounts for 10-50% of the total IR luminosity. We also find no measurable difference between the PAH luminosity ratios of $\mathrm{L_{11.3}/L_{7.7}}$ and $\mathrm{L_{6.2}/L_{7.7}}$ for the IRAGN and non-IRAGN, suggesting that AGN do not significantly excite or destroy PAH molecules on galaxy-wide scales. Interestingly, a small subset of galaxies (8 of 65 galaxies) show a strong excess of [O IV] $\lambda25.9\mu$m emission compared to their PAH emission, which indicates the presence of heavily-obscured AGN, including 3 galaxies that are not otherwise selected as IRAGN. The low PAH emission and low [Ne II] emission of the IRAGN and [O IV]-excess objects imply the IR luminosity of these objects is dominated by processes associated with the AGN. Because these galaxies lie in the "green valley" of the optical color-magnitude relation and have low implied SFRs, we argue their hosts have declining SFRs and these objects will transition to the red sequence unless some process restarts their star-formation.

Subject headings: galaxies: active — infrared: galaxies

1. INTRODUCTION

The mid-IR (3-19μm) spectrum of star-forming galaxies is dominated by strong emission features often associated with polycyclic aromatic hydrocarbons (PAHs). PAH molecules are made up of tens to hundreds of carbon atoms in planar lattices that typically are several Å in diameter (Leger & Puget 1984; Allamandola et al. 1985). Specifically, each PAH band is identified with specific carbon-carbon (C-C) and carbon-hydrogen (C-H) bending and stretching modes (Allamandola et al. 1989). Their vibrational modes are excited by efficient absorption of UV and optical photons whose energy is re-emitted in the IR. In many galaxies, the emission of young stars and active galactic nuclei (AGN) is almost entirely absorbed by dust and re-emitted in the IR; PAHs must then be used for detailed diagnostics of the luminosity sources.

The luminosity in the mid-IR PAH emission bands is very strong for galaxies with ongoing star-formation. The total PAH emission can contribute as much as 20% of the total IR luminosity and the 7.7μm PAH band may contribute as much as 50% of the total PAH emission (e.g., Smith et al. 2007). Certain PAH bands are made up of several dust emission features (e.g., 7.7μm, 8.6μm, 11.3μm, 12.7μm, and 17.0μm PAH bands) and so we will use the general term "feature" to describe the PAH emission bands.

From laboratory experiments, models of stochastic heating of dust grains predict that the relative strengths of PAH features are dependent on the size distribution of PAH grains and the ionization state of the PAH molecules (Schutte et al. 1993; Draine & Li 2001). Although the detailed physics is not well understood, existing models do explain the general trends observed for the various PAH features.

Previous *Spitzer* studies (Diamond-Stanic & Rieke 2010; O'Dowd et al. 2009; Smith et al. 2007) have found trends between the ratios of the various PAH features and galaxy properties, such as AGN activity and star formation history. A tendency for active galaxies to have lower ratios of the 6-8μm PAH features relative to the 11.3μm PAH feature has been reported both by

[1] George P. and Cynthia Woods Mitchell Institute for Fundamental Physics and Astronomy, and Department of Physics & Astronomy, Texas A & M University, College Station, TX 77843-4242; heath.shipley@tamu.edu
[2] Steward Observatory, University of Arizona
[3] National Optical Astronomy Observatory, Tucson, AZ
[4] Department of Physics & Astronomy, Siena College, Loudonville, NY 12211

O'Dowd et al. (2009) and Smith et al. (2007). Smith et al. argued that AGN are able to modify the PAH grain size distribution or are able to excite the emission of larger PAH molecules. O'Dowd et al. interpreted their results as being consistent with the destruction of smaller PAH grains by shocks or X-rays associated with the AGN, but were unable to determine a difference between AGN-dominated and AGN–starforming composite sources. Diamond-Stanic & Rieke (2010) chose a sample of local Seyfert galaxies to explore the effects of AGN on PAH emission. They found similar results to the previous studies when observing the AGN-dominated nuclear regions of galaxies, and determined AGNs do not excite PAH emission. In contrast, off-nuclear (presumably) star-forming regions in the galaxy disks had 7.7- to-11.3μm PAH ratios similar to those of star-forming galaxies in studies from the literature.

Here, we extend studies of IR luminous galaxies with mid-IR spectroscopy to higher redshifts and higher luminosities. Specifically, we focus on galaxies that have high IR luminosities ($> 10^{11} L_{\odot}$) and moderate redshifts ($z \lesssim 0.6$). This allows us to study the nature of the IR emission in galaxies at the same redshift range and IR luminosity range that dominate the IR luminosity density at high redshifts ($z \sim 1$ Le Floc'h et al. 2005). By observing the mid-IR spectral features of these galaxies we can therefore study the ionization state of the IR emission, and study how both star-formation and AGN contribute to the IR luminosity in these objects.

An additional goal of our study is to understand if there is a correlation (causal or otherwise) between the IR-active stages involving star-formation and/or AGN and other galaxy properties, such as their optical color. At a basic level the optical color depends on the galaxies' star-formation histories (galaxies with recent star-formation have bluer optical colors, and passive galaxies lacking any recent star-formation form a well documented "red sequence" e.g., Bell et al. 2004; Blanton et al. 2003; Faber et al. 2007). Studies of the optical colors of galaxies with high IR-luminosity (as measured by their MIPS 24μm emission) show they span a wide range of optical color from the blue star-forming galaxies, through the "green valley", and up to the blue edge of the red sequence (Bell et al. 2005; Mendez et al. 2013). This highlights a dependency of galaxy colors on IR activity. Wyder et al. (2007) show that the sequence of star-forming galaxies becomes redder with increasing optical luminosity, which is presumably a result of increased dust obscuration. This implies that stages of increased dust obscuration in luminous galaxies may be a precursor to the cessation of star-formation in galaxies as they migrate through the "green valley" to the quiescent red sequence (Faber et al. 2007), and this may be related to quenching by the presence of an AGN (Bundy et al. 2008; Nandra et al. 2007; Schawinski et al. 2007, 2010). Because IR-luminous galaxies have optical colors that span from the star-forming sequence to the red-sequence, there may be a relationship between their excitation mechanism (star-formation versus black hole accretion) and their optical color (Bell et al. 2005; Chen et al. 2010; Nandra et al. 2007).

To date samples of IR-luminous with mid-IR spectroscopy have been heterogeneous or incomplete in their coverage of galaxies over the full range of optical color. For our study, we allow for changes in the mid-IR spectral features as a function of optical color in galaxies by using a sample of IR-luminous galaxies that is selected to have a uniform distribution in rest-frame $(u-r)_{0.1}$[5] color. In sections 2 and 3, we describe our sample selection and ancillary data. In section 4, we describe our *Spitzer* IRS observations, data reduction, and analysis of the IRS spectra. In section 5, we describe our measurements of the total IR luminosity and discuss correlations between the PAH emission and emission from other atomic lines. In section 6, we discuss the color-magnitude relation for IRAGN, AGN effects of PAH emission, and the significance of [O IV] emission. In section 7, we present our conclusions. The ΛCDM cosmology we assume is $H_0 = 71$ km s^{-1} Mpc^{-1}, $\Omega_m = 0.27$, and $\Omega_\lambda = 0.73$ throughout this work.

2. SAMPLE DEFINITION AND SELECTION

Our main goal is to compare the mid-IR spectral properties of AGN and star-forming (SF) galaxies in luminous IR galaxies (LIRGs) out to moderate redshifts ($z \lesssim 0.6$). To accomplish this goal, we must be sensitive to the fact that both AGN and IR-luminous star-forming galaxies are known to span a broad range in optical color (see section 1). As discussed above, the energetics of both obscured AGN and star-forming galaxies may affect both the mid-IR spectral properties and the optical color. To avoid any bias related to these effects, we therefore built a sample of IR-luminous galaxies for spectroscopy that span an approximately uniform distribution of $(u-r)_{0.1}$ optical color that spans the full range from the blue, star-forming sequence to the red, quiescent sequence.

We built our primary sample for IRS spectroscopy using the AGN and Galaxy Evolution Survey (AGES, Kochanek et al. 2012). This survey provides deep ($I <$ 20 mag) spectroscopy covering the $\sim$10 deg^2 Boötes field, which includes deep optical imaging from the NOAO Wide Deep-Field Survey (NWDFS) (Jannuzi & Dey 1999). The field was also covered with *Spitzer*/IRAC imaging at 3.6–8.0 μm as discussed in Ashby et al. (2009), and with MIPS imaging at 24–160 μm first with shallow coverage by Houck et al. (2005) and subsequently with much deeper coverage as part of MIPS AGES (MAGES) survey (PI: B. Januzzi). The spectroscopy, optical, and mid-IR imaging allows us to select IR-luminous galaxies out to moderate redshift and over the full range of $(u-r)_{0.1}$ optical color.

As our parent sample, we selected 498 galaxies from the AGES data with spectroscopic redshifts $0.2 < z < 0.6$, and $f_\nu(24\mu\text{m}) > 1.2$ mJy. We then searched the *Spitzer* archive for programs that had previously targeted galaxies in our parent sample with IRS spectroscopy. Two programs satisfied our needs and included *Spitzer*/IRS data for a total of 17 galaxies from PID 20113 (PI: H. Dole) and 38 galaxies from PID 20128 (PI: G. Lagache); to our knowledge the data from these programs have not been published previously.

We supplemented the archival IRS spectroscopy with new IRS observations of additional galaxies taken as part

[5] Note that throughout, $(u-r)_{0.1}$ and $M(r)_{0.1}$ are the rest-frame color and absolute magnitude observed at z=0.1 (as used extensively in the SDSS literature, see, e.g., Blanton et al. 2003). Furthermore, throughout, $M(r)_{0.1}$ and $(u-r)_{0.1}$ are measured in AB magnitudes (Oke & Gunn 1983).

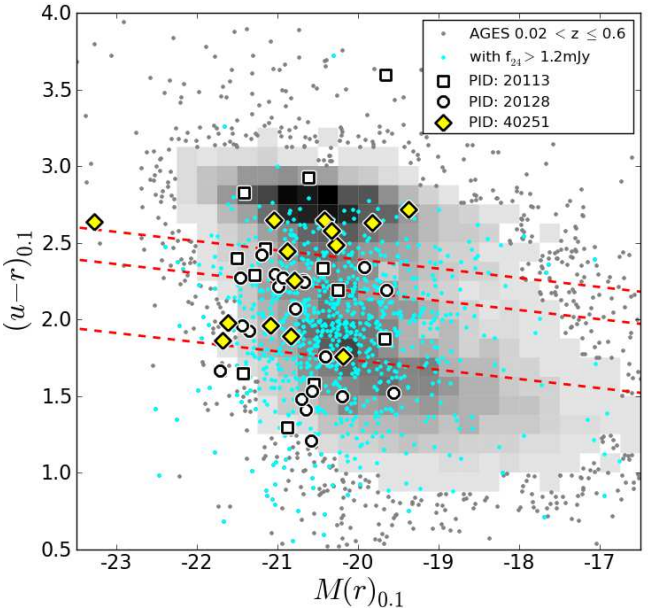

Figure 1. Color-Magnitude Diagram using optical data from the AGES catalog for our sample. The grey-shading indicates the density of all galaxies from AGES in that region of color-magnitude space and $0.02 < z < 0.6$, where the grey-shading increases as the density increases linearly. The cyan points show those AGES sources with $0.02 < z < 0.6$ and $f(24\mu\mathrm{m}) \geq 1.2$ mJy, the IRS spectroscopic limit for our sample. The galaxies selected in our sample are indicated by white squares, white circles, and yellow diamonds for Dole (program 20113), Lagache (program 20128, non-FLS sources), and Rieke (program 40251), respectively. Furthermore, we selected IR-luminous galaxies for our sample such that they span the full range of $(u-r)_{0.1}$ optical color with an equal number (12-13) galaxies in each of four bins, denoted by the red-dashed lines and defined in section 2.

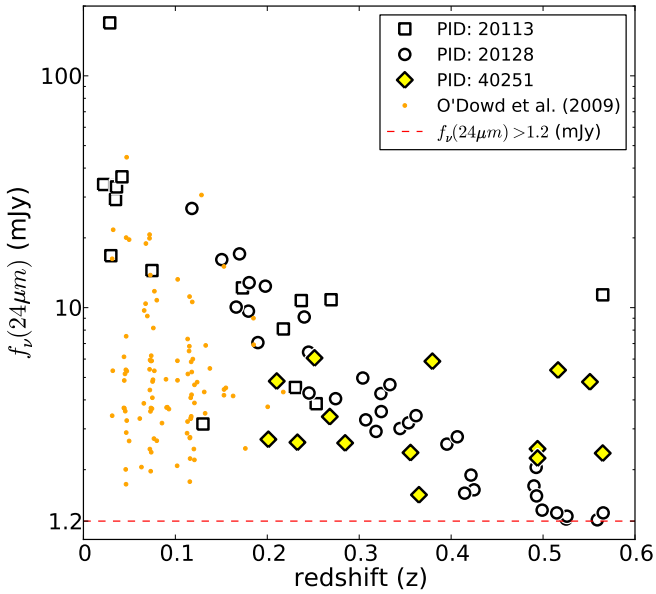

Figure 2. Distribution of the redshifts and 24μm flux densities of the 65 galaxies in our IRS sample. The galaxies are indicated by white squares, white circles, and yellow diamonds for Dole (program 20113), Lagache (program 20128), and Rieke (program 40251), respectively. The orange circles are from O'Dowd et al. (2009) sample as a comparison to our sample. The red dashed line indicates $f_\nu(24\mu\mathrm{m}) = 1.2$mJy. The redshift mean and median of the distribution are 0.30 and 0.28, respectively. The redshift distribution is fairly uniform from $0.2 < z < 0.6$, with an interquartile range (which contains the inner 50% of galaxies) of $z_{\mathrm{interquartile}} = 0.18 - 0.42$.

of the MIPS guaranteed time observations (GTO) 40251 (PI: G. Rieke) to ensure that our full IRS sample includes galaxies with an approximately uniform distribution in $(u-r)_{0.1}$ color. To identify the sample for GTO observations, we derived bins in $(u-r)_{0.1}$ optical color that run roughly parallel to the red sequence, which has some slope in the color-magnitude plane:

$$\begin{aligned}(u-r)_{0.1} + 3/50 \times (M[r]_{0.1} + 20) &> 2.39\\ 2.39 \geq (u-r)_{0.1} + 3/50 \times (M[r]_{0.1} + 20) &> 2.18\\ 2.18 \geq (u-r)_{0.1} + 3/50 \times (M[r]_{0.1} + 20) &> 1.73\\ (u-r)_{0.1} + 3/50 \times (M[r]_{0.1} + 20) &\leq 1.73,\end{aligned}$$

We require at least 12 galaxies in each of these color bins. As shown in figure 1, this required new IRS observations of 14 additional galaxies from our GTO allocation in PID 40251.

The combined archival IRS data (7 + 19 galaxies) and new IRS data (14 galaxies) yield a sample of 40 galaxies that form our primary IRS sample. In addition, the archival programs used here include 29 additional galaxies, either at lower redshift ($0.02 < z < 0.2$; 12 galaxies) or from the *Spitzer* First Look Survey (FLS; 17 galaxies), or both. These galaxies appear to all be selected using a 24 μm flux limit ($f_\nu(24\mu\mathrm{m}) > 1.2$ mJy). We included these galaxies as a secondary sample here because our sample is increased by ∼70% and it enables us to extend our observations to both lower-luminosity objects (in the case of the objects at $0.02 < z < 0.2$) and adds higher luminosity objects from the FLS (even though these have no $(u-r)_{0.1}$ color information). As discussed in section 4.2, we ultimately exclude four observations (two from AGES and two from the FLS) that showed contamination from a serendipitous source in the IRS slit. Therefore, our full sample of primary and secondary sources includes 65 galaxies with $f_\nu(24\mu\mathrm{m}) > 1.2$ mJy and $0.02 < z < 0.6$.

In summary, we have three samples defined in this paper.

- Full Sample. All 956 galaxies with $f_\nu(24\mu\mathrm{m}) > 1.2$ mJy and redshift of $0.02 < z < 0.6$ in AGES.
- Parent Sample. All 498 galaxies with $f_\nu(24\mu\mathrm{m}) > 1.2$ mJy and redshift $0.2 < z < 0.6$, from which targets for new IRS observations were selected.
- IRS Sample. The 65 galaxies with $f_\nu(24\mu\mathrm{m}) > 1.2$ mJy that have IRS spectroscopy either from archival data (51 galaxies) or our new GTO observations (14 galaxies).

Figure 1 shows the $(u-r)_{0.1}$–$M(r)_{0.1}$ color-magnitude diagram for all the galaxies in AGES in the redshift range of our full sample, and indicates the galaxies in the redshift range with ($f_\nu(24\mu\mathrm{m}) > 1.2$ mJy (956 galaxies). The figure shows that the existing galaxies from the *Spitzer* archival programs (non-FLS galaxies) are biased toward IR-luminous galaxies with blue colors compared to the AGES sample and the sample of GTO observations help to uniformly distribute the galaxies in $(u-r)_{0.1}$ color. The properties of our sample are listed in table 2

and figure 2 shows the redshift and 24μm flux density distributions.

3. *Spitzer* IMAGING DATA

3.1. *Boötes Field*

For our IRS sample, we used observations taken from the Infrared Array Camera (IRAC) and MIPS. IRAC observations were taken from the *Spitzer* Deep Wide-Field Survey (SDWFS) catalog for Boötes sources (Ashby et al. 2009). The sources in our sample had IRAC coverage in all four photometric IRAC bands (3.6μm, 4.5μm, 5.8μm, and 8.0μm). We used the 8.0μm selected SDWFS catalog for the four IRAC band magnitudes (given in the Vega magnitude system) of the Boötes sources.[6]

Since our IRS data were acquired, deeper MIPS data were taken as part of the MIPS AGES (MAGES) program (B. Jannuzi et al., in prep). These data catalogs provide deeper imaging in all three MIPS bands, (24 μm, 70 μm, and 160 μm) in the Boötes field. The MAGES catalogs provide significantly deeper imaging at 70 μm and 160 μm, achieving detections at these wavelengths for many of the sources in our IRS sample.

Using the MAGES data catalog, we first matched all 50 galaxies (in the AGES Boötes' field) with a $r = 2''$ matching radius at 24 μm. For all galaxies, the IRS integrated 24 μm flux densities (see section 4.2) agreed within the measurement errors with those matched to the MAGES 24 μm flux densities. We then used the MAGES matched catalog to obtain 70 μm and 160 μm flux densities for sources in our IRS sample, including 46 galaxies with 70 μm detections and 27 galaxies with 160 μm detections (flux densities given in table 2). We use these longer wavelength data to improve our estimates of the total IR luminosity (see section 5.2).

3.2. *Spitzer First Look Survey (FLS)*

Sources in our IRS sample from the *Spitzer*/FLS have IRAC and MIPS imaging from programs published in the literature. We used data from the four IRAC channels from the *Spitzer* data archive provided from Lacy et al. (2005). We used the combined FLS catalog to acquire the four IRAC band flux densities of the FLS sources. We converted the flux densities to the appropriate magnitudes (Vega magnitude system), identical to that for the Boötes sources. We use the catalogs of Papovich et al. (2006) and Frayer et al. (2006) to obtain MIPS 24μm flux densities, and MIPS 70μm and 160μm flux densities, respectively.

3.3. *IRAC AGN Selection*

The primary goal of this study is to compare the mid-IR spectral features of IR-luminous galaxies with indications of AGN activity to those without. IR-selected AGN can be identified from "star-forming" IR galaxies because AGN typically show indications of warm ($\sim$1000 K) dust heated by the AGN which produces a characteristic power law continuum through the IRAC channels (e.g., Donley et al. 2012). We take advantage of this color selection here to identify IR-selected AGN using the color selection criteria proposed by Stern et al. (2005). The Stern et al. color selection is defined using spectroscopic observations of galaxies in the same redshift range as our sample, which makes it appropriate here. This selection is also relatively immune to mis-identification of purely star forming galaxies as AGN over the redshift range of our study (Donley et al. 2008), so this region in the diagram can be re-interpreted to identify galaxies where the AGN makes a substantial contribution to the mid-IR output but is not totally dominant (Mendez et al. 2013). We show the result of this selection on our IRS spectroscopic sample in figure 3.

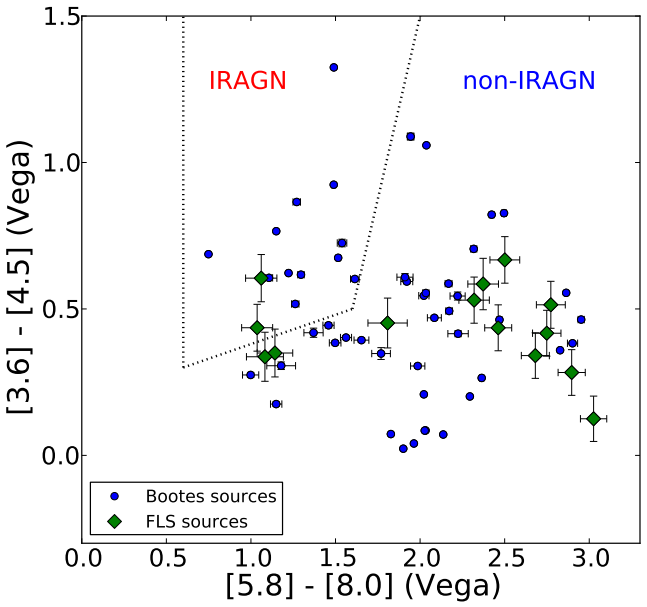

Figure 3. IRAC colors of [5.8] - [8.0] versus [3.6] - [4.5] for galaxies in our IRS sample. Here, the IRAC colors are in the Vega magnitude system, following Stern et al. (2005). The blue circles are sources from the Boötes field and green diamonds are FLS sources. The dotted lines show the empirical selection-criteria for IRAC-AGN selection: galaxies inside this "wedge" are IRAC-selected AGN (Stern et al. 2005). We denote the subsample of galaxies in our IRS sample that satisfy these colors as IRAGN. We denote galaxies outside this wedge as non-IRAGN, and we expect the IR emission in these objects to be dominated by star-formation.

We define the subsample of galaxies in our IRS sample that satisfy this IRAC color-color selection as IRAGN. This includes 14 out of the 65 galaxies in our IRS sample (2 are in the FLS sample and 12 are in the AGES Boötes sample). Based on the statistics from Stern et al. (2005), it is unlikely that our IRAGN subsample contains any star-forming galaxies for the AGES sample. It is likely, however, that our subsample of IRAGN is incomplete for all AGN in our sample. Furthermore, the number of AGN dominated galaxies in our sample may be biased towards a higher fraction because of our 24μm selection criteria. For the remainder of this paper we refer to galaxies in our sample satisfying this selection as IRAGN, and the other galaxies in our sample as non-IRAGN. We expect the non-IRAGN subsample to be dominated by star-forming galaxies even though some will have an AGN.

[6] Throughout we use [3.6], [4.5], [5.8], and [8.0] to denote the magnitudes with respect to Vega measured in each IRAC band, respectively.

4. IRS OBSERVATIONS, DATA REDUCTION, AND ANALYSIS

4.1. *IRS Observations*

The IRS was used in staring mode to make the observations with both the low-resolution short-low (SL) and long-low (LL) IRS modules, giving 5.2-38.0μm coverage (SL $\sim$ 5.2-14μm and LL $\sim$ 14-38μm) with resolving power of $\sim 60-125$. Exposure times were estimated based on the 24 μm flux densities and the purpose of the individual programs. Observing times ranged from 360-600 seconds for the SL observations and 180-3600 seconds for the LL observations. The SL and LL modules have respective slit widths of $\sim$3.7" and $\sim$10.5", the slits have physical sizes of 1.5-25 kpc and 4.3-70 kpc respectively, over the redshift range of the sample ($0.02 < z < 0.6$). At the median redshift, the physical slit sizes are 16 kpc and 45 kpc, respectively.

4.2. *Data Reduction*

We used the two-dimensional *Spitzer* data products processed by the *Spitzer* Pipeline version S18.7.0 to perform the standard IRS calibration. Our post-pipeline reduction of the spectral data started from the pipeline products basic calibrated data (bcd) files. To perform sky subtraction, we created a sky frame for each object by taking the median of all the images for a single object at the same nod position. We subtracted this image from the frames for the other nod position for the object to produce sky subtracted images. We combined all sky subtracted images for each object at a given nod position to produce coadded 2-dimensional images. We used IRSCLEAN (v.1.9) on each image to remove and correct for bad and rogue pixels.

We used the *Spitzer* IRS Custom Extractor (SPICE) software to extract one-dimensional spectra for each order at each nod position. We chose to use the optimal extraction with point-source calibration because it improved the signal-to-noise (S/N) ratios for our sources. We combined the 1D spectra manually using a weighted mean for the nod position for each order. We combined the SL2 + SL1 orders (for the 25 sources with SL2 data) and LL2 + LL1 orders (for all sources).

To combine the SL and LL orders we took care to match the flux calibration, accounting for light lost outside the spectroscopic slits (which varies considerably between SL and LL, see above). We integrated the IRS spectra from the SL module with the IRAC 5.8μm and the IRAC 8.0μm transmission functions, and we integrated the spectra from the LL module with the MIPS 24μm transmission function. We took the ratio of the observed flux density as measured directly from the IRAC and MIPS observations to the flux density synthesized from the IRS spectra as an aperture correction (although other effects may contribute to variations in the IRS flux density) for each spectrum, with mean corrections of 1.55, 0.98, and 1.12 for IRAC 5.8μm, IRAC 8.0μm, and MIPS 24μm respectively. We combined (using a weighted mean, weighting by inverse variance) the flux-corrected spectra to produce a single 1D spectrum for each source covering the entire wavelength range.

During the process of the IRS data reduction, we rejected four galaxies from our sample because these objects show strong contamination from another source in the slit, resulting in a dubious spectrum. After rejecting these galaxies, our IRS sample includes IRS spectra of 67 objects used in the spectral analysis. However, two of our sources were repeat visits of the same source (sources observed both by the 20113 Dole and 20128 Lagache programs). Comparing the reduced spectra for each of these sources, they give consistent results for redshift and PAH ratios. For the analysis here, we rejected the visits with lower S/N. Therefore, our final dataset includes IRS spectra for 65 unique objects.

4.3. *IRS Spectral Fitting*

To study the mid-IR emission features in the IRS spectra of our sample, we used the PAHFIT spectral decomposition code (Smith et al. 2007), designed for *Spitzer* IRS data. PAHFIT uses a χ^2 minimization routine to fit a non-negative combination of multiple emission features and continua to the one-dimensional spectra of our sources. The features included in PAHFIT are the dust emission features from PAHs (modeled as Drude profiles), thermal dust continuum, continuum from starlight, atomic and molecular emission lines (modeled as Gaussians), and dust extinction. The PAH emission features at (e.g. 7.7, 11.3, and 17 μm) are blends of multiple components, and PAHFIT treats these complexes as individual emission "features".

We used PAHFIT to fit the IRS spectrum for each galaxy in our sample. The line fluxes derived by PAHFIT for the emission features for each object are listed in Tables 3 and 4. Figure 4 shows the PAHFIT spectral decompositions for the spectra of objects ID=4 and 23 in our sample, using the IDs in Table 2. Object 4 is classified as an IRAGN as described by the method in Section 3.3, while object 23 shows no indication of an AGN. The spectra are characteristic of the data quality and fit quality of our sample.

We fit the IRS spectra for the galaxies in our sample using PAHFIT models with and without dust extinction. PAHFIT uses a model where the dust is mixed with the emitting stars and grains, as opposed to an absorbing screen. Our fits showed that the PAHFIT χ^2 values are improved using models with dust extinction for 60/65 galaxies in our sample (the other 5 galaxies had similar χ^2 values and are low S/N sources). Other studies have also found it desirable to use the default PAHFIT dust extinction parameter (Smith et al. 2007; O'Dowd et al. 2009; Wu et al. 2010; Diamond-Stanic & Rieke 2010). Therefore, we chose to use results from PAHFIT for our sample that include dust extinction. However, none of our conclusions are changed if we use the fits excluding dust extinction.

Using PAHFIT, we also fit for the redshift of each galaxy using the IRS spectra. All galaxies in our sample have a measured redshift from optical spectroscopy from AGES in the Boötes sample (Kochanek et al. 2012) or from Papovich et al. (2006) in the FLS sample, but the PAHFIT measurement provides an independent check on the redshift, and provides supporting evidence that the mid-IR source corresponds to the optical counterpart. PAHFIT requires an input redshift (it does not minimize over redshift as part of the fit). Therefore, for each galaxy in our sample we used PAHFIT with a grid of redshift. We did this step iteratively. We first ran PAH-

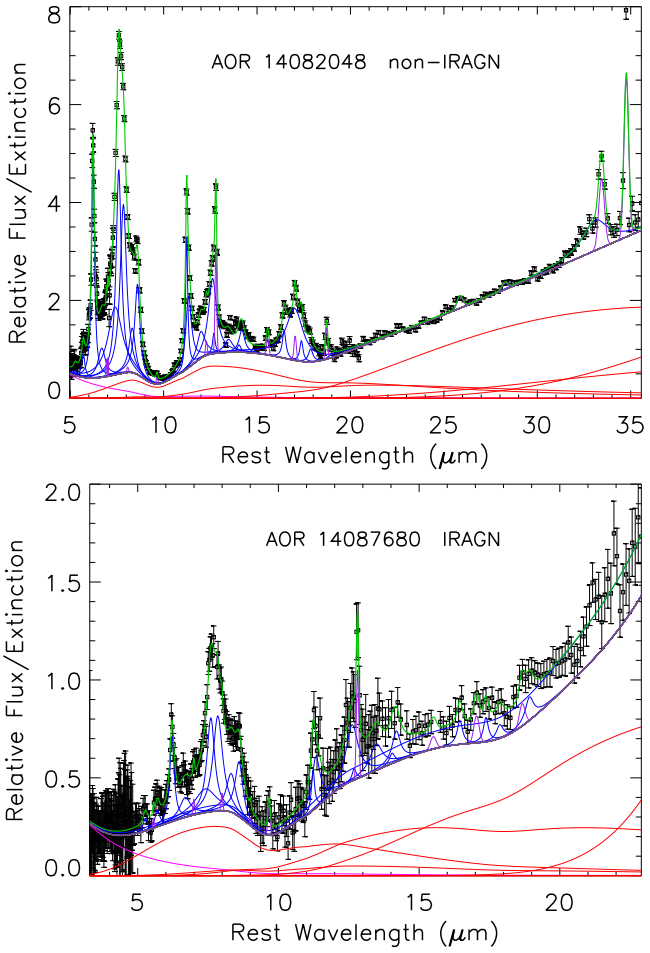

Figure 4. Examples of PAHFIT spectral decomposition to object 23 (top) and object 4 (bottom). In each panel, the IRS spectroscopic data are shown as black squares. The total fit and individual spectral components fit by PAHFIT are shown, including the molecular and atomic emission features (blue curves), dust continua (red), and stellar light (magenta). The total fit (the sum of all the model components) is shown in green, which provides a good representation of the data.

FIT using a the full redshift range with $0.0 < z < 0.6$ with steps of $\Delta z = 0.01$, and we selected the fit with the best reduced χ^2. We then refined the redshift solution by fitting the redshift with $\Delta z = 0.001$ using a redshift range ± 0.1 about the best-fit redshift from the first step.

We verified the consistency in our redshifts by doing a comparison to the AGES optical redshifts. We found the two redshifts for all galaxies agree within 2%, the resolution of the IRS. Table 2 gives both the redshift measured from the optical spectroscopy and the redshift measured independently from the IRS spectrum here.

4.4. *Offset Between IRS SL and LL Modules*

In the analysis below, one of the important emission-line ratios we will consider is the relative strength of the 7.7 μm to 11.3 μm PAH features. For galaxies with $z < 0.2$, these lines both sit in the IRS SL module, but for $z \geq 0.2$, the 11.3 μm feature shifts into the LL module, in which case the two lines are measured from different modules with different slit widths. Our procedure to flux-calibrate the spectra using the IRAC and MIPS photometry described above should account for changes in the relative flux owing to the slit widths. Nevertheless, we did some additional tests to confirm that the flux measured for the 11.3 μm feature is accurate.

The median redshift of our IRS sample is $z_{\rm median} = 0.28$, and therefore, nearly 50% of the galaxies in our IRS sample have the 11.3 μm feature in the LL module. For approximately one quarter of the sample ($0.19 < z < 0.28$), the 11.3 μm feature lies in the overlap region covered by both the SL and LL modules. For these galaxies, we compared the measured emission of this feature in the SL and LL modules separately, and found that for 13/16 galaxies there was less than a 3% difference in the measured flux of the feature. For the remaining three galaxies, the features have lower signal-to-noise, and the difference in the fluxes is within the uncertainties on the measurement. Therefore, we are confident that the uncertainties are fully represented in the errors on the data, and that any systematic errors from our flux calibration from using the two modules are small.

5. COMPARISON OF MID-IR EMISSION FEATURES AND RELATION TO TOTAL INFRARED LUMINOSITY

5.1. *Composite Spectra*

The spectra of the IRAGN and non-IRAGN subsamples show different continua and strength of emission features, as illustrated in Figure 5. The figure shows composite spectra for the full sample (IRAGN + non-IRAGN), the IRAGN, and non-IRAGN. The composite spectra were created by performing a weighted mean. First, the spectra were interpolated to a common wavelength spacing using the observed wavelength scale of each order for the SL and LL modules ($\Delta\lambda$(SL2) $\approx$ 0.030μm, $\Delta\lambda$(SL1) $\approx$ 0.059μm, $\Delta\lambda$(LL2) $\approx$ 0.083μm, $\Delta\lambda$(LL1) $\approx$ 0.166μm) to preserve the information from each spectrum when creating the composite spectrum. The composite spectra are then normalized to the continua fluxes at 21μm. An outset panel of each composite spectrum is shown for the [O IV] λ25.9μm emission line. For the [O IV] panel, we have subtracted the continuum out (by fitting a line to the continuum around the [O IV] line for each composite spectrum) to better show the strength of the [O IV] line for the IRAGN compared to the non-IRAGN. The [O IV] atomic line at 25.89μm has been established to be an indicator of AGN luminosity by Meléndez et al. (2008) and Rigby et al. (2009) by comparison to hard (E > 10 keV) X-rays. Diamond-Stanic et al. (2009) showed that this line can be used to find AGN that are in heavily dust-obscured galaxies and therefore are missed by optical, X-ray, and other selection criteria.

The IRAGN composite spectrum shows a lower PAH emission equivalent width compared to the non-IRAGN composite spectrum. The most apparent PAH emission feature in the IRAGN subsample is the weak 7.7 μm feature. The continuum is mostly flat across the wavelength range of the spectra, suggesting the continuum is raised in response to heating from the AGN. Furthermore, the PAH features are not absent in the IRAGN, which suggests that in part, the mid-IR continuum from the AGN is diluting the luminosity from the PAH features. In comparison, the continuum is much weaker in the non-IRAGN composite spectrum, and this spectrum shows very prominent PAH and other emission features throughout the wavelength range covered.

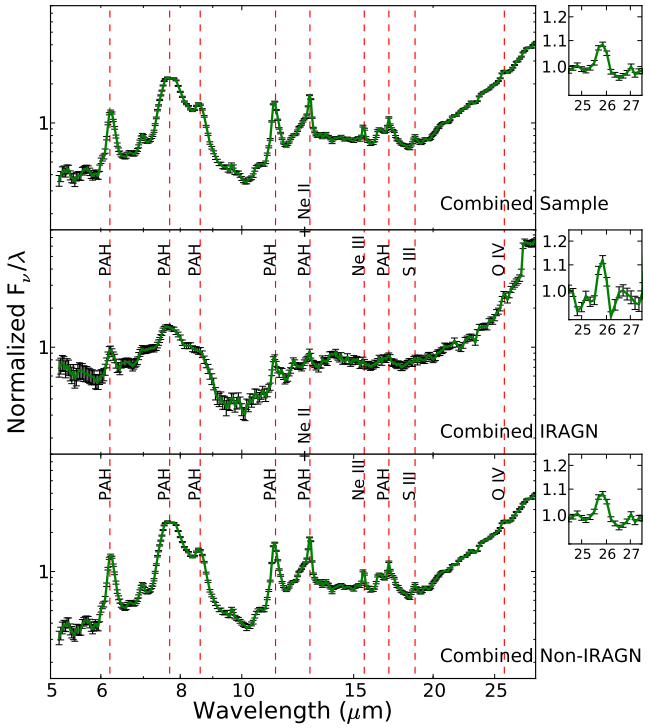

Figure 5. Composite spectra for the IRS sample. The top panel shows the composite spectrum for all 65 galaxies in the IRS sample. The middle and bottom panels show composite spectra for the subsamples of IRAGN (14 galaxies) and non-IRAGN (51 galaxies), respectively. The vertical red-dashed lines indicate the prominent PAH features and emission lines in the wavelength range, as labeled. The flux is normalized at the continuum flux of 21μm. The outset panels show the composite spectra in a small wavelength region 24.5μm-27.5μm to show the strength of the [O IV] λ25.9μm emission line (see section 5.1 for explanation). The error bars shown is the error on the weighted mean for each composite spectrum.

5.2. *Measuring the Total Infrared Luminosity*

We used model spectral energy distributions (SEDs) to estimate the total $L_{IR} = L_{8-1000\mu m}$ from the MIPS 24μm flux densities for all sources. 70μm and 160μm flux densities were used when available from MAGES for Boötes sources and Frayer et al. (2006) for the FLS sources. To calculate the total IR luminosity, we tested several model libraries that provide far-IR SEDs that vary in shape as a function of galaxy IR luminosity and ionization (Dale & Helou 2002; Chary & Elbaz 2001; Rieke et al. 2009). For galaxies with 24 and 70 μm detections, or 24, 70, and 160 μm flux densities, the total IR luminosities are consistent (within 40%) using any of the IR SEDs from Chary & Elbaz (2001), Dale & Helou (2002), or Rieke et al. (2009). However, because 19 galaxies (including four IRAGN) in our sample are detected at only 24 μm, we use the Rieke et al. (2009) IR SEDs because our tests showed that the total IR luminosities derived using their templates with only the 24 μm are closest with those derived from multiple MIPS bands (24 and 70 μm, or 24, 70, and 160 μm). These tests are described more fully in Appendix A. For the four IRAGN only detected at 24μm, we interpret the luminosities from the purely star-forming spectral templates to be upper limits. However, if we assume an extreme case of a quasar (using the quasar SED templates of Shang et al. 2011) then our total IR luminosity is at most overestimated by a factor of 3.5 for these four IRAGN. However, we consider this highly unlikely because the MIPS-to-IRAC flux ratios for these four IRAGN ($F_{24\mu m}/F_{8.0\mu m} = 4.2$ median) is highly discrepant from the optically luminous quasars of Shang et al. (2011) ($F_{24\mu m}/F_{8.0\mu m} = 1.4$ median) and so this factor of 3.5 is a very conservative limit for this extreme case. We believe our estimates of the total IR luminosity to be valid due to the majority of our sample being LIRGs and having modest redshifts, based on the work of Rujopakarn et al. (2013).

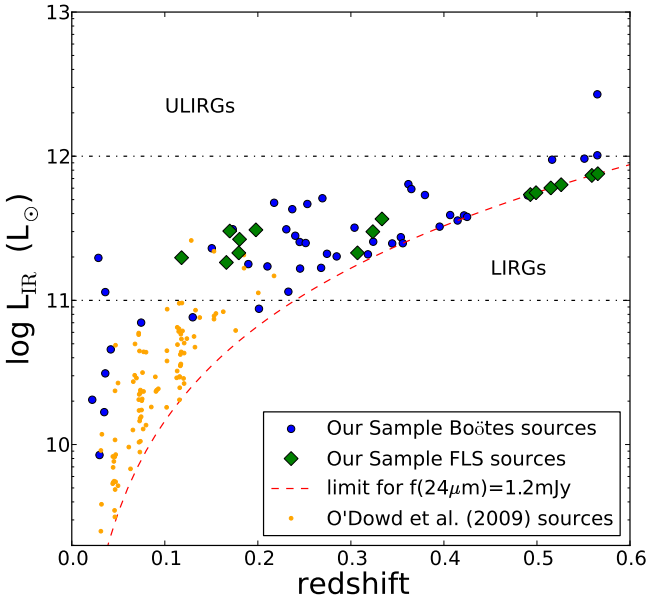

Figure 6. Redshift versus the total IR luminosity from 8-1000μm for our IRS sample (blue circles, Boötes sources; green diamonds, FLS sources) derived from the MIPS 24 μm data (and 70 and 160 μm, if available) derived using the Rieke et al. (2009) IR SEDs. The galaxies in our IRS sample span the range of IR luminosity of "Luminous IR galaxies" (LIRGs), $L_{IR} = 10^{11} - 10^{12} L_\odot$. The figure also shows the O'Dowd et al. (2009) SSGSS sample (orange circles), which are lower redshift and IR luminosity. The dashed curve shows the limiting IR luminosity as a function of redshift for a fixed 24 μm flux density of 1.2 mJy using the IR SEDs from Rieke et al. (2009).

Figure 6 shows the calculated total IR luminosities from fits to the MIPS data using the Rieke et al. (2009) IR SEDs. Table 2 lists the MIPS flux densities for 24μm, 70μm, and 160μm, along with the total IR luminosities. The figure also shows the relation for the IRS sample of the *Spitzer* SDSS Galaxy Spectroscopic Survey (SSGSS) from O'Dowd et al. (2009), which illustrates the distinction in IR luminosity and redshift range between their sample and our sample here.

5.3. *Contribution of PAH Emission to L_{IR}*

In figure 7, we show the distribution of L_{PAH}/L_{IR} for the entire sample (bottom panel), the subsamples of IRAGN (middle panel) and non-IRAGN (top panel). Here L_{PAH} is the sum of all the luminosities of the PAH features at 6.2, 7.7, 8.6, 11.3, 12.7, and 17.0 μm, and L_{IR} is the total IR luminosity as described in section 5.2 using the Rieke et al. (2009) templates. The median ratio of L_{PAH}/L_{IR} is 0.08 with an interquartile range (which contains the inner 50% of galaxies) of 0.05 to 0.11. We find that L_{PAH}/L_{IR} is higher in the non-IRAGN sample,

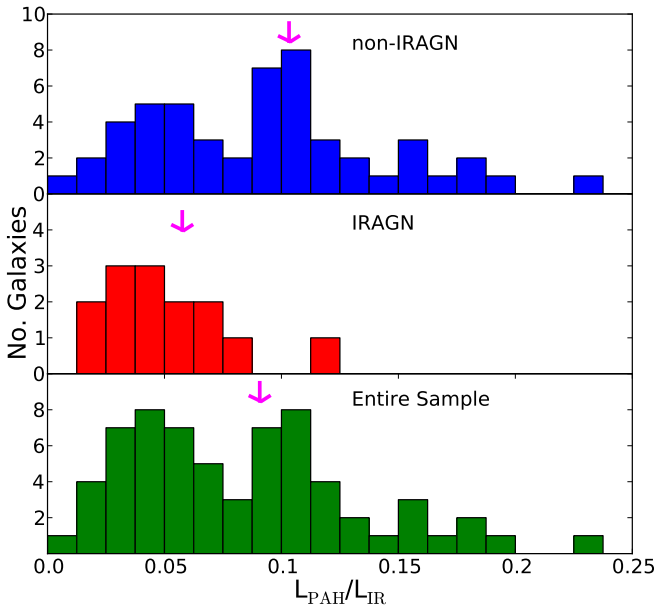

Figure 7. The distribution of L_{PAH}/L_{IR} for our sample, where L_{PAH} is the total luminosity of the 6.2, 7.7, 8.6, 11.3, 12.7, and 17.0μm PAH emission features. The bottom panel shows the distribution for our IRS sample. The middle panel shows the distribution for our subsample of IRAGN, and the top panel shows the distribution for our subsample of non-IRAGN. The median L_{PAH}/L_{IR} is 0.05 for the IRAGN, and is about half that for the non-IRAGN which have a median of $L_{PAH}/L_{IR} = 0.09$. The arrows represent the L_{PAH}/L_{IR} ratios from the composite spectra in figure 5 ($L_{PAH}/L_{IR} = 0.09$, 0.06, and 0.10 for the IRS sample, IRAGN, and non-IRAGN, respectively).

with a median of 0.09, compared to $L_{PAH}/L_{IR} = 0.05$ for the IRAGN. A K-S test applied to the distributions gives a D-statistic = 0.52, which indicates a 99.7% likelihood that the IRAGN and non-IRAGN have different parent distributions. If we exclude the four IRAGN only detected at 24μm and not in the far-IR, the K-S test gives a D-statistic = 0.49 and a likelihood of 97.6%.

The 7.7μm feature for either IRAGN or non-IRAGN contributes significantly to the entire amount of PAH emission. The median $L_{7.7}/L_{PAH}$ is 0.45 with an interquartile range (which contains the inner 50% of galaxies) of 0.40 to 0.48 for our sample; and the median IRAGN $L_{7.7}/L_{PAH}$ is slightly higher at 0.49. These results show that as much as 10% of the total IR luminosity can come from the 7.7μm feature alone.

The IRAGN in our sample show lower L_{PAH}/L_{IR} compared to the non-IRAGN, where 13/14 IRAGN have $L_{PAH}/L_{IR} < 0.09$. This is similar to the findings of Smith et al. (2007), who suggested there may be a natural limit to the absolute PAH strength in sources with AGNs, either because of partial destruction of the grains or an increase to the total infrared luminosity from other continuum sources. However, there are two key differences between our sample and that of Smith et al. (2007). First, the objects in our sample have (in most cases) significantly higher IR luminosities. Second, the IRS apertures encompass the integrated light from the galaxies in our sample, whereas the IRS resolves those in the Smith et al. (2007) sample to include light separately from the disk and nucleus. This will tend to dilute the effects of the AGN on the integrated PAH ratios. We discuss this further in section 6.2.

Table 1
Emission Feature Detection Frequencies

Feature/Line	All galaxies	non-IRAGN galaxies	IRAGN galaxies
6.2μm	41/65 63%	37/51 73%	4/14 29%
7.7μm	47/65 72%	42/51 82%	5/14 36%
8.6μm	44/65 68%	40/51 78%	4/14 29%
11.3μm	49/65 75%	42/51 82%	7/14 50%
12.7μm	37/65 57%	36/51 71%	1/14 7%
17.0μm	19/65 29%	18/51 35%	1/14 7%
[Ne II]	46/65 71%	43/51 84%	3/14 21%
[Ne III]	22/65 34%	20/51 39%	2/14 14%
[O IV]†	22/56 39%	14/45 31%	8/11 73%

Note. — We present our detection frequencies for the most common PAH emission features and atomic emission lines in the mid-IR for the IRS sample. Each column gives the frequency that a given emission feature is detected at $\geq 3\sigma$ significance in the full sample, or the IRAGN, or the non-IRAGN subsamples (given as number of galaxies with detections in the sample or as a percentage of galaxies with detections compared to their respective sample, see section 5.4). In the far left column, atomic features are labeled, and PAH features are denoted by their central wavelengths. †9 sources in our sample have redshifts ($z \gtrsim 0.5$) for which [O IV] is shifted out of the IRS LL channel and are not included in the sample for this line.

5.4. *Detection Frequency of Emission Features*

Figure 8 shows the fraction of galaxies in our sample whose IRS spectra show some of the most common emission features detected at $\geq 3\sigma$ significance. Emission frequencies are given in table 1 for the full sample, non-IRAGN, and IRAGN subsamples. As an example, the 7.7μm PAH emission feature is found with $\geq 3\sigma$ significance in only 5 out of the 14 IRAGN in our the sample, and therefore its frequency is 36%. Although a variety of factors can influence detection of the PAH features, since our sample is selected primarily on mid-IR flux, to first order we should reach similar detection limits on average for all the sample members.

The 6.2μm, 7.7μm, 8.6μm, 11.3μm, and 12.7μm PAH features are present in more than 50% of the galaxies in our sample (and the same PAH features are present in more than 70% of the non-IRAGN galaxies). The most commonly detected PAH emission feature is the 11.3μm feature with a frequency of 75%. The PAH feature with the lowest detection frequency (29%) is the 17μm feature. Considering the two subsamples, the frequency of the PAH emission features for the IRAGN subsample is less than half that of the non-IRAGN subsample except for the 11.3μm feature, which has 50% for IRAGN and 82% for the non-IRAGN. This supports the conclusion from Diamond-Stanic et al. (2009) that the 11.3μm feature is relatively unaffected by AGN.

Figure 8 shows the frequency that the [Ne II] λ12.8μm, [Ne III] λ15.6μm, and [O IV] λ25.9μm emission lines are detected with $\geq 3\sigma$ significance in our IRS sample. The emission line of [Ne II] is a tracer of the SFR (Ho & Keto 2007), while the ratio of [Ne III]/[Ne II] and the [O IV] emission line trace harder ionization parameters that correlate with AGN intrinsic luminosity (e.g. Diamond-Stanic et al. 2009; Meléndez et al. 2008; Rigby et al. 2009). The [Ne II] line has a >80% detection frequency for the non-IRAGN subsample, signifi-

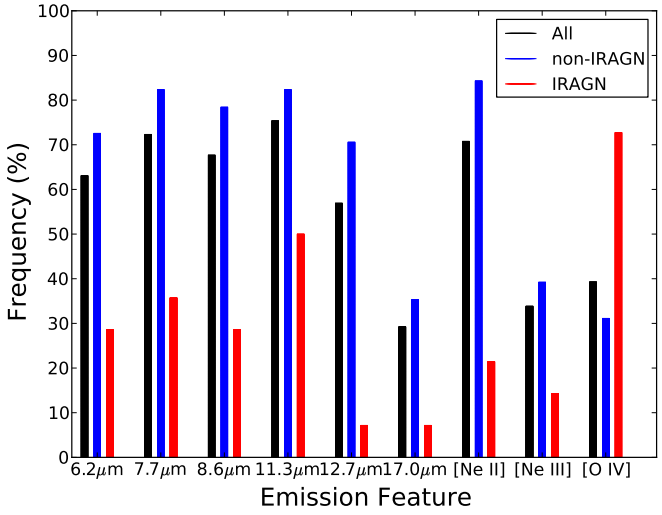

Figure 8. Detection frequencies for common mid-IR PAH features and atomic emission lines in the IRS sample. Each histogram gives the frequency that a given emission feature is detected at $\geq 3\sigma$ significance in the IRS sample (black bars), or the IRAGN (red bars) or the non-IRAGN (blue bars) subsamples. On the abscissa, atomic features are labled, and PAH emission features are denoted by their central wavelengths.

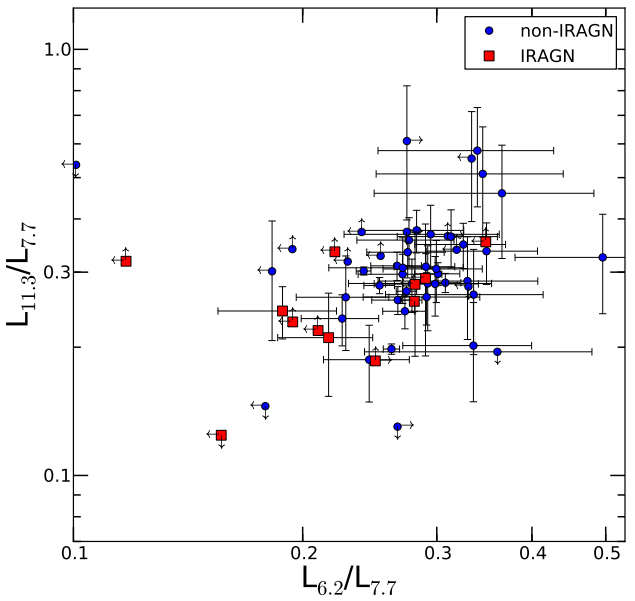

Figure 9. PAH band ratios $L_{6.2}/L_{7.7}$ vs. $L_{11.3}/L_{7.7}$ for the galaxies in the IRS sample. The $L_{6.2}/L_{7.7}$ ratio is a tracer of PAH grain size, and the $L_{11.3}/L_{7.7}$ ratio is a tracer of PAH grain ionization (O'Dowd et al. 2009). The red squares denote IRAGN and the blue circles denote non-IRAGN galaxies. The IRS sample falls mostly within the locus defined by 0.2–0.4 in both axes. This shows that the galaxies have a mixture of grain sizes and different ionization fractions of PAHs. We measure a weak correlation between $L_{6.2}/L_{7.7}$ and $L_{11.3}/L_{7.7}$ (Spearman's $\rho = 0.41$), which we interpret as evidence for decreasing PAH grain size and increasing ionization within the locus. We also observe that the IRAGN ratios are slightly lower typically compared to the non-IRAGN galaxies, in our IRS sample.

cantly higher than the ∼20% detection frequency for the IRAGN subsample. In contrast, the [O IV] line has >70% detection frequency in the IRAGN subsample compared to ∼30% for the non-IRAGN. These detection frequencies of [Ne II] and [O IV] are independent of the selection of these subsamples (which depend solely on their IRAC colors), yet give additional evidence that the emission from these samples stems from star-formation (in the case of the non-IRAGN) and AGN (in the case of the IRAGN). We discuss the inferred physics based on the [Ne II] and [O IV] emission lines in Sections 5.8 and 6.4.

5.5. *Measures of Grain Sizes and Ionization State*

Models show that the relative power emitted in the different PAH emission features depends on the distribution of molecular grain sizes contributing to that PAH feature (Draine & Li 2001; Schutte et al. 1993; Tielens 2005). Generically, the models predict that PAH molecules of smaller size should emit more power at shorter wavelengths and PAH molecules of larger size should emit more power at longer wavelengths (i.e., the emission from the 6.2μm PAH feature should be dominated by grains of smaller size than those at 11.3μm). Therefore, the ratio of the strength of longer–wavelength PAH features to shorter–wavelength PAH features constrains the size of the PAH molecules.

In addition, the models predict that the ionization state of PAH molecules affects the relative luminosity in each PAH emission feature (Draine & Li 2001). For example, the C-C vibrational modes are expected to be more intense in ionized PAH molecules (Tielens 2005). The 6.2μm and 7.7μm bands result from radiative relaxation of C-C stretching modes and the features should change little relative to each other as the ionization fraction changes (O'Dowd et al. 2009). In contrast, the power of the PAH bands attributed to C-H modes such as the 11.3μm and 12.7μm features is expected to decrease (moving from neutral to ionized clouds in the interstellar medium (ISM)). Therefore, the ratio of the strength of ionization–independent PAH features, such as the 6.2 and 7.7 μm feature, to ionization–dependent PAH features, such as the 11.3 and 12.7 μm features should be sensitive to the overall ionization state of the PAH molecules.

Therefore, the PAH molecule sizes and ionization state can be constrained by comparing the PAH band ratios $L_{6.2}/L_{7.7}$ to $L_{11.3}/L_{7.7}$. The former traces PAH grain size, but is relatively unaffected by ionization. The latter is sensitive to ionization and less affected by changes in grain size. Figure 9 shows these line ratios for the galaxies in our sample. The sample lies mostly in a locus between line ratios of 0.2–0.4 for both $L_{6.2}/L_{7.7}$ and $L_{11.3}/L_{7.7}$. This is consistent with the findings from other studies (O'Dowd et al. 2009; Diamond-Stanic & Rieke 2010; Wu et al. 2010). We measure a weak correlation between $L_{6.2}/L_{7.7}$ and $L_{11.3}/L_{7.7}$ (Spearman's $\rho = 0.41$), which we interpret as evidence for decreasing PAH grain size with increasing ionization within the locus (this is consistent with the trend seen in O'Dowd et al. 2009).

5.6. *Relation between Radiation Hardness and PAH Strength*

The emission-line ratio of the [Ne III] (15.6μm with an ionization potential of 41eV) emission to the [Ne II] (12.8 μm, with an ionization potential of 21.6eV) is a measure of the hardness of the radiation field (Smith et al. 2007). Figure 10 shows the ratio of $L_{[NeIII]}/L_{[NeII]}$ as a

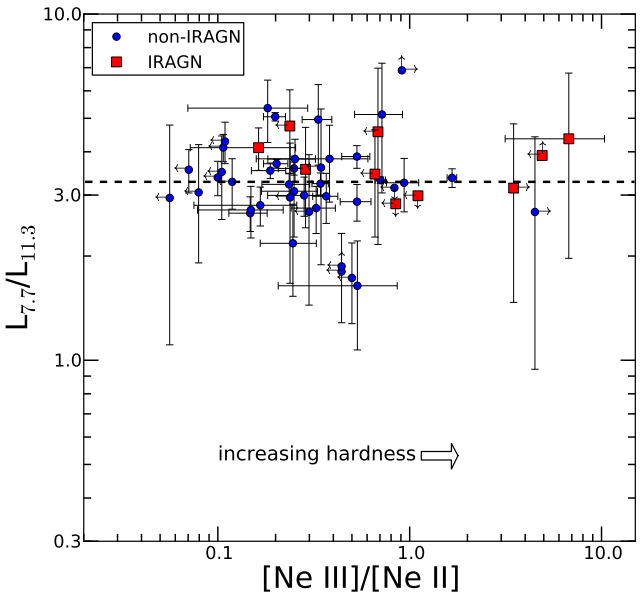

Figure 10. [Ne III]$_{15.6\mu m}$/[Ne II]$_{12.8\mu m}$ versus $L_{7.7}/L_{11.3}$. Blue circles show the subsample of non-IRAGN, and red squares show the subsample of IRAGN (not all IRAGN have [Ne III]/[Ne II] ratio detections). The dashed line is the median $L_{7.7}/L_{11.3}$ value for the non-IRAGN subsample only. There is no trend between [Ne III]/[Ne II] and $L_{7.7}/L_{11.3}$ for either the non-IRAGN or IRAGN. This is similar to the conclusions from other studies (O'Dowd et al. 2009; Wu et al. 2010), but contrasts with the findings of Smith et al. (2007), although we expect this difference, in part, is due to issues with the full integrated light (nucleus and outer regions from the galaxies in our IRS sample fall within the IRS aperture in constrast to the sample of Smith et al. 2007).

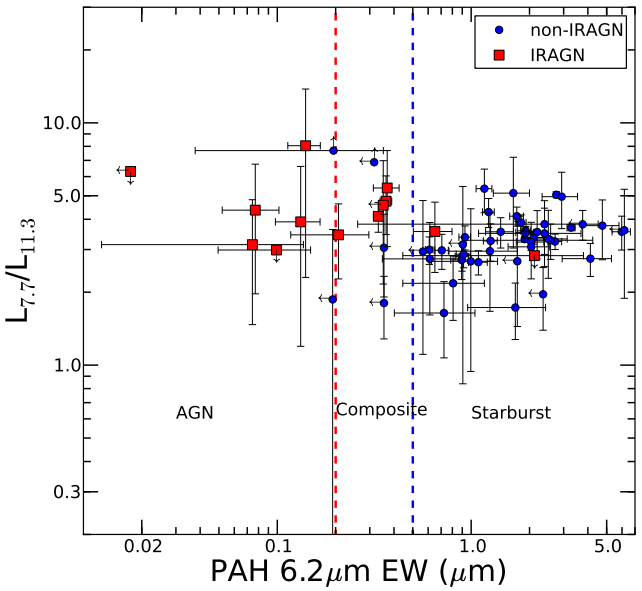

Figure 11. PAH 6.2μm equivalent width versus the $L_{7.7}/L_{11.3}$ PAH ratio. The dashed lines show selection criteria to separate sources into AGN, composite, and SB galaxies, as labeled in the figure. Galaxies with EW $\leq$ 0.2 μm are likely AGN (red-dashed line), galaxies with EW $>$ 0.5 μm are SB galaxies (blue-dashed line), and galaxies that fall between these lines are likely AGN+SB composites. We observe no correlation between $L_{7.7}/L_{11.3}$ and the EW of the 6.2μm PAH feature.

function of $L_{7.7\mu m}/L_{11.3\mu m}$, which is an indicator of the ratio of ionized-to-neutral PAH molecules, as discussed in section 5.5. In general, there is no correlation between $L_{[NeIII]}/L_{[NeII]}$ and $L_{7.7\mu m}/L_{11.3\mu m}$. The dashed line in figure 10 shows the median $L_{7.7\mu m}/L_{11.3\mu m}$ for the non-IRAGN only. There is tentative evidence that the IRAGN have $L_{7.7\mu m}/L_{11.3\mu m}$ ratios higher than this median, but this is not statistically significant given our sample size.

We see no IRAGN galaxies with extremely low $L_{7.7\mu m}/L_{11.3\mu m}$ ratios (<1), as seen in the Smith et al. (2007) sample. The $L_{7.7\mu m}/L_{11.3\mu m}$ ratio behavior contrasts strongly with Smith et al. (2007), but is in reasonable agreement with others (Wu et al. 2010; O'Dowd et al. 2009). We suspect the difference is a result of the fact that the IRS spectra for our sample contains the integrated light from the galaxy (nucleus + galaxy), whereas the IRS apertures containing the nuclei used by Smith et al. (2007) included only the galactic nuclear regions. Our sample contains few sources with high hardness ratios ([NeIII]/[NeII] > 2, similar to the samples of O'Dowd et al. 2009; Smith et al. 2007; Wu et al. 2010), and most sources with high hardness ratios are upper limits only. This suggests that higher hardness ratios cannot account for the trend seen by Smith et al. (2007). This conclusion agrees with that in Gordon et al. (2008) from a study of H II regions in M101 and Brandl et al. (2006) studying 22 starburst galaxies. Diamond-Stanic & Rieke (2010) showed that spectra taken from an off-axis region of an AGN host galaxy have no significant differences from SINGS H II galaxies' PAH ratios. As discussed in Section 5.4, the 11.3μm feature is relatively unaffected by AGN, which could explain the lower ratios seen by Smith et al. (2007). The other studies also have samples that would remain relatively unchanged over their respective ranges of hardness ratios (O'Dowd et al. 2009; Wu et al. 2010, $z_{med} = 0.08$ and normal SF galaxies and $0.008 < z < 4.27$, respectively).

5.7. *The Distribution of the 6.2μm PAH Equivalent Width*

Previous studies use the equivalent width (EW) of the 6.2μm PAH feature to classify sources as AGN, starbursts (SBs), and composite AGN+SB subsamples (e.g., Wu et al. 2010). Sources where an AGN dominates the IR emission are expected to have lower 6.2μm PAH EW either because the mid-IR continuum from the AGN is much stronger and washes out the emission, or because the ionization field of the AGN destroys the PAH molecules, or a combination of the two. The EW measures the relative strength of the PAH feature to the mid-IR continuum, thereby allowing us to quantify the effects of an AGN.

Figure 11 shows the PAH 6.2μm EW versus the 7.7–to–11.3μm PAH flux ratio. The red dashed line shows a selection for AGN with EW $\leq$ 0.2μm, the blue dashed line shows a selection for SB galaxies with EW > 0.5μm, and AGN+SB composite sources populate the region between these regions (Armus et al. 2007). Most of the IRAGN (defined by the IRAC color-color selection) have low 6.2μm EW: 12 of the 14 IRAGN satisfy either the composite or AGN 6.2μm PAH EW criteria. Similarly, most of the non-IRAGN have high 6.2μm EW: 46 of 51 non-IRAGN satisfy the SB 6.2μm PAH EW criterion. Interestingly, the figure shows no correlation between the

6.2μm EW and $L_{7.7\mu m}/L_{11.3\mu m}$ ratio. A similar observation is shown for the $L_{7.7\mu m}/L_{11.3\mu m}$ ratio compared to the hardness of the radiation field in figure 10 (see section 5.6). Therefore, we see no indication that the presence of an AGN affects the $L_{7.7\mu m}/L_{11.3\mu m}$ ratio. If the AGN were photoionizing the PAH molecules; and reducing the 6.2μm EW, we would expect the $L_{7.7\mu m}/L_{11.3\mu m}$ ratio to decrease with decreasing 6.2μm EW. Because we do not, we conclude that the AGN decreases the PAH 6.2μm EW because the AGN increases the mid-IR continuum, and not because the AGN destroys the PAH molecules on a galaxy wide scale (see section 6.3).

5.8. *The relationship between PAH luminosity, Star-formation Rate, and AGN luminosity*

As discussed above, the [Ne II] and the [O IV] emission lines are useful probes of the SFR and AGN luminosity, respectively. In figure 12, we plot the flux measured in the [Ne II] and [O IV] lines against the summed flux from the 7.7μm and 11.3μm PAH features, which we are able to then compare directly against results from Diamond-Stanic & Rieke (2010). The [Ne II] emission correlates strongly with PAH emission, with a Spearman correlation coefficient of $\rho = 0.94$ and a linear fit of $F([\text{Ne II}]) = 0.02 \times {F_{7.7+11.3}}^{0.99}$. The scatter in the [Ne II]–PAH relation increases for fainter fluxes, which may be related to the presence of IRAGN, which are more frequent in the sample at faint line fluxes.

In contrast, the [O IV] line shows almost no correlation with PAH emission, with a Spearman correlation coefficient of $\rho = 0.19$. Because [Ne II] correlates so well with the PAH emission, the relation in figure 12 suggests that the PAH emission correlates with the SFR. This is consistent with the findings of Diamond-Stanic & Rieke (2010) and Genzel et al. (1998). We also do not see any clear difference between the IRAGN and non-IRAGN in either the [Ne II] or [O IV] versus PAH emission plot in figure 12, indicating further that the PAH features are likely tracing star formation in both subsamples, and that the presence of AGN do not increase (or decrease) PAH emission integrated over galaxies (Diamond-Stanic & Rieke 2010).

The bottom panel in figure 12 shows a swath of eight galaxies with low PAH emission and high [O IV] emission. These galaxies lie above the upper dashed line, which is 4 times greater than the fit to the non-IRAGN (lower dashed line). Approximately one-half (5/11[7]) of the IRAGN have [O IV] emission above this line. In addition, three of the galaxies above this line are non-IRAGN. Removing these galaxies from the sample shows a correlation may be present (Spearman's $\rho = 0.60$) for galaxies without strong [O IV] emission. As stated in Section 3.3, the Stern et al. (2005) IRAC color-color method used to identify IRAGN selects more broad-line AGN, but only about 40% of narrow-lined AGN. Because excess [O IV] indicates the presence of ionization from an AGN, these three non-IRAGN galaxies likely harbor heavily-obscured AGN that are missed by the IRAGN selection.

[7] Three do not have [O IV] detections due to the redshift of the source.

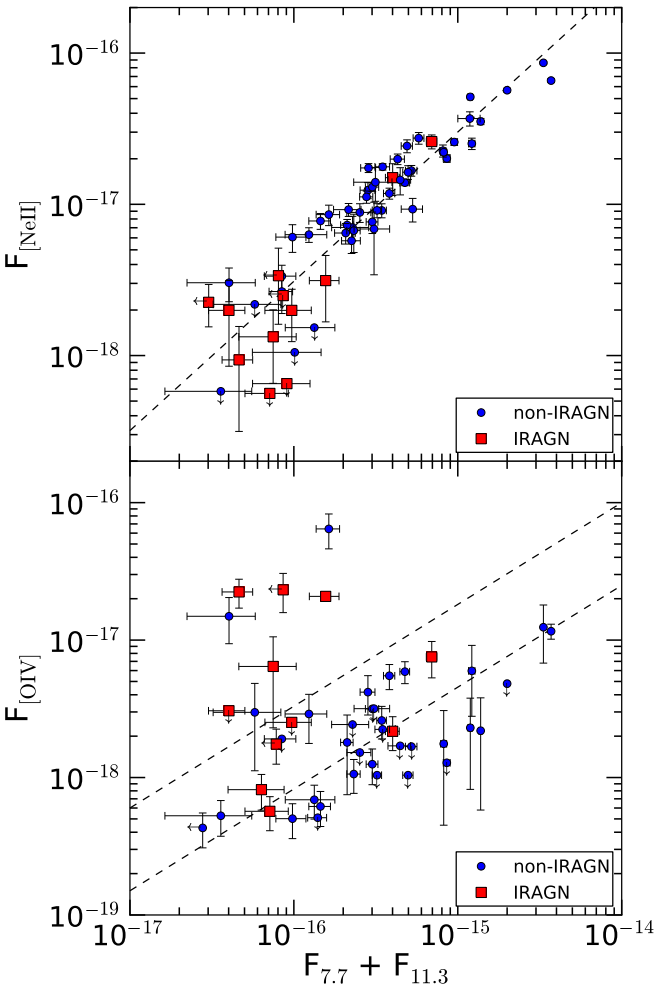

Figure 12. The relationship between the PAH emission features and the [Ne II] (top panel) and [O IV] (bottom panel) emission lines. All units are in W/m^2. The top panel shows a correlation between the PAH emission and [Ne II] emission line suggesting PAH emission correlates with star formation. The dashed line represents a linear fit ($0.02\times{F_{7.7+11.3}}^{0.99}$) to the sample. The bottom panel shows that there is little, if any, correlation between PAH emission and [O IV], but there is a population of objects with low PAH emission and excess [O IV] emission. The upper dashed line is four times greater than the fit to the non-IRAGN subsample (lower dashed line) used to select the [O IV]-excess objects.

6. DISCUSSION

6.1. *The Color-Magnitude Diagram for IR Luminous Galaxies*

Because our IRS sample spans a nearly uniform distribution in optical color, we are able to study differences in the IR emission properties of galaxies with different positions on the optical color-magnitude relation. For the full sample (all galaxies in AGES with $f(24\mu m) > 1.2$ mJy and $0.02 < z < 0.6$, including both the IRAGN and non-IRAGN), we find the median values are $M(r)_{0.1}$ = -20.36 mag and $(u-r)_{0.1} = 1.97$ mag. These differ from the median values for our IRS sample, which are $M(r)_{0.1}$ = -20.74 mag and $(u-r)_{0.1} = 2.23$ mag). We attribute these differences to the fact that our IRS sample has a uniform selection in $(u-r)_{0.1}$ optical color whereas the full sample is weighted toward bluer $(u-r)_{0.1}$ optical colors. In figure 13, we replot the location of the IR-luminous

galaxies on the optical $M(r)_{0.1}$ versus $(u-r)_{0.1}$ color-magnitude diagram, and we denote galaxies by their IR luminosity as derived from their MIPS data (see section 5.2) in coarse bins of luminosity: low-luminosity galaxies ($L_{IR} = 10^{10} - 2.4 \times 10^{11}$ $L_\odot$), medium-luminosity ($L_{IR} = 2.4 \times 10^{11} - 4.5 \times 10^{11}$ $L_\odot$) and high-luminosity ($L_{IR} > 4.5 \times 10^{11}$ $L_\odot$), evenly splitting the medium and high luminosity bins (∼100 galaxies for each bin) for the full sample to improve the statistics for comparison[8]. Using the full sample of galaxies with $f(24\mu m) > 1.2$ mJy, we find no difference in $(u-r)_{0.1}$ color as a function of IR luminosity. Each of the three IR luminosity bins have nearly equal median colors $(u-r)_{0.1} = 2.0$ mag with similar interquartile ranges. The only difference we measure is that the $(u-r)_{0.1}$ color distribution of the highest IR luminosities is slightly broader than for the lower luminosity galaxies.

In comparison, our IRS sample shows the low, medium and high-luminosity galaxies are also mostly distributed evenly in the color-magnitude relation. We observe slight evidence that the $(u-r)_{0.1}$ color *decreases* for *increasing* IR luminosity. We find the median $(u-r)_{0.1}$ colors are 2.34 mag, 2.25 mag, and 1.96 mag for the low, medium, and high-luminosity galaxies, respectively. However, we consider this trend not to be significant given the lack of any correlation in the full sample.

We compared the $(u-r)_{0.1}$ color distributions for galaxies classified as IRAGN and non-IRAGN from the full sample of galaxies with $f(24\mu m) > 1.2$ mJy from AGES (cyan points in figure 13). The median values, $M(r)_{0.1} \sim$ -20.34 mag and $(u-r)_{0.1} \sim 2.00$ mag for the IRAGN and for the non-IRAGN $M(r)_{0.1} \sim$ -20.36 mag and $(u-r)_{0.1} \sim 1.96$ mag are similar. A K-S test applied to the distributions gives a D-statistic = 0.06 and a likelihood of 74.8%, which we interpret as evidence that there is no difference between the $(u-r)_{0.1}$ colors for IR luminous galaxies selected as IRAGN and non-IRAGN.

Considering only our IRS sample, the IRAGN span the range from the blue cloud to the red sequence, where 67% (8 of 12) are located in the "green valley" or the red sequence ($(u-r)_{0.1} + 3/50 \times (M[r]_{0.1} + 20) > 2.18$). The distribution of $(u-r)_{0.1}$ color for the non-IRAGN galaxies appears shifted toward bluer colors compared to the IRAGN. We find that the median $(u-r)_{0.1}$ color for the non-IRAGN is 2.13 mag compared to the median color for the IRAGN, 2.38 mag, shown in figure 13. However, because we see no difference between IRAGN and non-IRAGN in the full sample of IR luminous galaxies, we do not consider these differences significant.

Other studies of the optical colors for AGN have found that they populate a similar region of the color-magnitude relation compared to our IRAGN samples here (Nandra et al. 2007; Weiner et al. 2007). While our IRAGN span a similar $(u-r)_{0.1}$ color range as X-ray selected AGN (e.g. Nandra et al. 2007), so do the non-IRAGN. So it is unclear if the presence of an AGN is driving redder $(u-r)_{0.1}$ colors in our IRS sample of IR luminous galaxies. Therefore, in galaxies selected to be IR luminous (with $f(24\mu m) > 1.2$ mJy), there is no measurable difference between the optical $(u-r)_{0.1}$ colors for galaxies selected as IRAGN and non-IRAGN.

[8] If we use the traditional ULIRG identification ($L_{IR} > 10^{12} L_\odot$) for the full sample, we have only 9 galaxies for comparison.

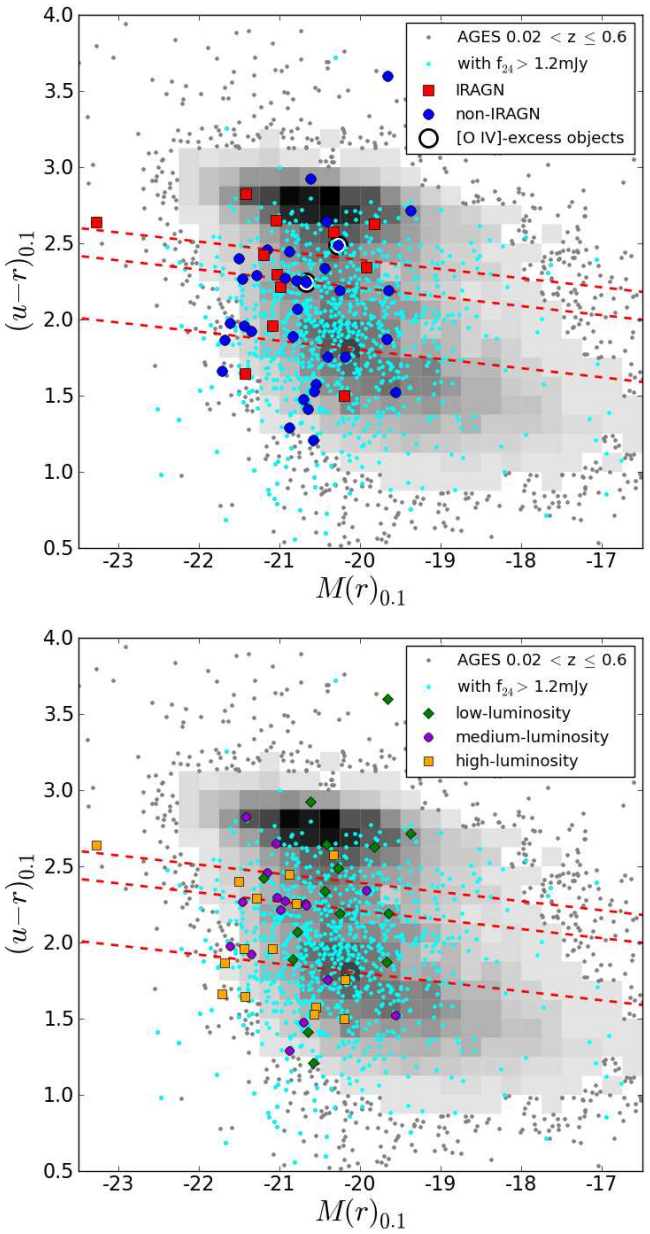

Figure 13. Optical $(u-r)_{0.1}$ color-magnitude diagram. Both plots are similar to figure 1 except for symbol changes to the Boötes IRS sample. (*Top Panel*) The sample symbols denote IRAGN (red squares), non-IRAGN (blue circles), and non-IRAGN galaxies with excess [O IV] (defined in section 5.8, black open circles). (*Bottom Panel*) The sample symbols denote galaxy IR luminosity as low-luminosity galaxies ($L_{IR} = 10^{10} - 2.4 \times 10^{11}$ $L_\odot$, green diamonds), medium-luminosity galaxies ($L_{IR} = 2.4 \times 10^{11} - 4.5 \times 10^{11}$ $L_\odot$, purple circles), and high-luminosity galaxies ($L_{IR} > 4.5 \times 10^{11} L_\odot$, orange squares).

However, there is a difference in our interpretation of the $(u-r)_{0.1}$ colors for the IRAGN and non-IRAGN. Most of the IRAGN in our IRS sample have low [Ne II] and PAH luminosities, which may imply they have significantly lower SFRs compared to the non-IRAGN (figures 12 and 14). Therefore, the fact that the IRAGN in our samples lie in the "green valley" or red sequence may imply they have declining SFRs or a recent cessation of star-formation, similar to conclusions reached

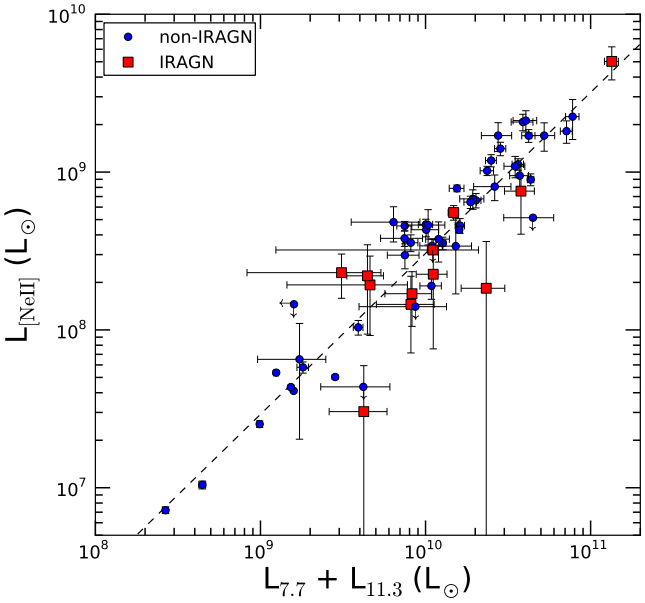

Figure 14. The relationship between the luminosity of the PAH emission features and the [Ne II] emission line. The [Ne II] luminosity correlates strongly with the PAH luminosity, with a Spearman correlation coefficient of $\rho = 0.90$ and a linear fit (dashed line) of $\mathrm{Log(L[Ne\ II])} = 1.02 \pm 0.03 \times \mathrm{Log(L_{7.7+11.3})} - 1.71 \pm 0.25$.

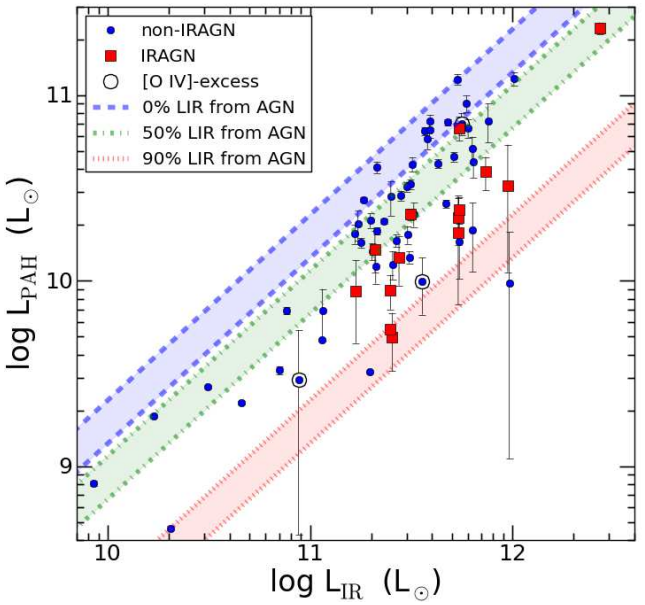

Figure 15. The total IR luminosity versus the PAH luminosity as an indicator for the contribution of AGN luminosity to the L_{IR}. The shaded regions represent percent amounts, marked in the plot, for the contribution of AGN luminosity to the total IR luminosity for the IRAGN in our sample under the assumption that the PAH luminosity traces the total SFR (see section 6.2 for explanation).

by Nandra et al. (2007). This also implies that star-formation is not a necessary component for an AGN to persist.

6.2. *AGN effects on PAH Emission and AGN contribution to L_{IR}*

Previous studies have used anticorrelations in the [Ne III]/[Ne II] versus $L_{7.7\mu m}/L_{11.3\mu m}$ ratios (see figure 10) to conclude that galaxies with an increasing hardness of radiation field from an AGN have relatively less emission from shorter wavelength PAH features compared to longer wavelength PAH features (e.g. Smith et al. 2007; O'Dowd et al. 2009; Wu et al. 2010). One interpretation is that the smaller PAH molecules are preferentially destroyed in the presence of the AGN (Smith et al. 2007; O'Dowd et al. 2009). It is certainly the case that AGN do not *increase* PAH emission, as shown in figure 12 (see also Diamond-Stanic & Rieke 2010).

In our sample, the luminosity for all PAH features is uniformly weaker in the IRAGN galaxies compared to the non-IRAGN and uniformly less frequent (see figures 5 and 8). Figure 5 shows that the mid-IR SEDs of the IRAGN in our sample show a weakly rising continuum with increasing wavelength (with possible silicate absorption at 9.7μm). Figure 12 shows that most of the IRAGN galaxies in our sample have low [Ne II] emission and PAH emission. Therefore, the IRAGN appear to have lower implied SFRs. Taken together, the data suggest that the reason IRAGN in our sample have lower PAH emission is a combination of higher mid-IR continuum from processes associated with the AGN combined with intrinsically lower SFRs. It is unclear if the AGN actually destroy PAH molecules but given the low [Ne II] fluxes, it seems more likely the lack of PAH emission is because the hosts of IRAGN have lower SFRs. It is possible that some other feedback mechanism from the AGN affects the SFR. We also have to be cautious about the selection effect for IRAGN that the AGN will boost the flux at 24μm and will select on a lower star-formation threshold than a purely star-forming sample. Thus, this may result in weaker observed PAH emission for the IRAGN.

Figure 14 shows that the PAH luminosity correlates linearly with the [Ne II] luminosity (linear fit of $\mathrm{Log(L[Ne\ II])} = 1.02 \pm 0.03 \times \mathrm{Log(L_{7.7+11.3})} - 1.71 \pm 0.25$). Because the correlation is linear, we conclude that both are good tracers of the total SFR (Ho & Keto 2007). We can then use the PAH luminosity and total IR luminosity to estimate the contribution of star-formation and AGN luminosity to the total IR luminosity for the IRAGN in our sample. In figure 15, we show our estimated contribution of AGN luminosity to the total IR luminosity for the IRAGN. We make the implicit assumption that the non-IRAGN galaxies with the highest L_{PAH}/L_{IR} ratios have no contribution from AGN luminosity to their L_{IR}. Under this assumption the contribution of AGN to the IR luminosity is a lower limit, and could be higher by a *systematic* amount. However, the relative contribution of an AGN to the IR luminosity is robust under this assumption. Using this premise, we define our 0% AGN luminosity contribution for the IRAGN by fitting the range of the L_{PAH}/L_{IR} ratios for the upper quartile of non-IRAGN galaxies with $L_{IR} \geq 10^{11} L_\odot$ using a unity relation between the two luminosities. The shaded region represents the range of scatter in our sample as to which galaxies are completely star-forming. Using this definition, we attribute 50-90% of the total IR luminosity in the IRAGN to an AGN rather than star-formation (a similar result to Schweitzer et al. 2006, from a study of QSOs), except for one object where the AGN contributes $< 50\%$ of the total IR luminosity (and has one of the highest [Ne II] luminosities of the IRAGN). While star-formation is a significant contribution to the

total IR luminosity for the IRAGN, the AGN is the dominant source of IR luminosity in these galaxies.

6.3. *Emission ratios of Short-to-Long wavelength PAHs in IRAGN and non-IRAGN*

O'Dowd et al. (2009) showed that the AGN in their sample have significantly lower $L_{7.7\mu m}/L_{11.3\mu m}$ values than the SF galaxies (similar to conclusions from Wu et al. 2010). Both O'Dowd et al. and Wu et al. found no significant difference in the $L_{6.2\mu m}/L_{7.7\mu m}$ ratio going from galaxies dominated by star-formation to those dominated by an AGN. Taken together, these observations suggest that galaxies with AGN show a reduction in the emission of shorter wavelength PAHs relative to longer wavelength PAHs. In contrast, we see no difference in either the $L_{7.7\mu m}/L_{11.3\mu m}$ or $L_{6.2\mu m}/L_{7.7\mu m}$ ratio for the IRAGN and non-IRAGN in our sample. Here we discuss possible reasons for the differences seen between the samples.

As noted above, previous studies argued that the smaller dust grains responsible for the shorter wavelength PAH molecules are preferentially destroyed in the presence of an AGN (Smith et al. 2007; O'Dowd et al. 2009; Wu et al. 2010). Diamond-Stanic & Rieke (2010) investigated possible destruction of PAH grains by AGN-driven shocks as X-ray heating was shown not to be as important as shock excitation (Roussel et al. 2007). While the effects of AGN-driven shocks on the observed PAH emission are complex and uncertain, one possible effect is that shocks leave uneven structures in the surviving dust grains that do not contribute to the PAH emission. However, Diamond-Stanic & Rieke (2010) noted that the molecules responsible for the 11.3μm feature are not strongly suppressed by shocks, and this can explain the observed lower $L_{7.7\mu m}/L_{11.3\mu m}$ ratios.

Diamond-Stanic & Rieke (2010) also found that AGN-dominated sources (the nuclei of local Seyfert galaxies) with low $L_{7.7\mu m}/L_{11.3\mu m}$ ratios have strong H_2 emission (H_2 S(3) rotational line at 9.67μm) indicating the presence of shocks[9]. This is consistent with observations of Roussel et al. (2007) and Smith et al. (2007) who observe stronger H_2 emission and lower $L_{7.7\mu m}/L_{11.3\mu m}$ ratios in local galaxies with AGN from SINGS. We do not have many sources with detected H_2 emission in the 9.67μm line (10/65 galaxies have H_2 flux detections at $\geq 3\sigma$). This suggests that, if shocks are present, they may not be strong enough to modify the short-to-long PAH ratios observed or to produce strong emission in this H_2 line.

As our sample has the highest median redshift (z_{med} = 0.28) of other recent studies (O'Dowd et al. 2009; Wu et al. 2010, z_{med} = 0.08 and z_{med} = 0.144, respectively) we view more integrated light from a galaxy and this may result in a significant difference not associated with the effects of an AGN. The discussion above only takes into account the differences seen between active galaxies and SF galaxies in short-to-long PAH ratios. As O'Dowd et al. (2009) discuss, the age and evolution of metallicity in a galaxy can also have an effect on the observed short-to-long PAH ratios.

[9] refer to Diamond-Stanic & Rieke (2010) for further description of other studies with similar results

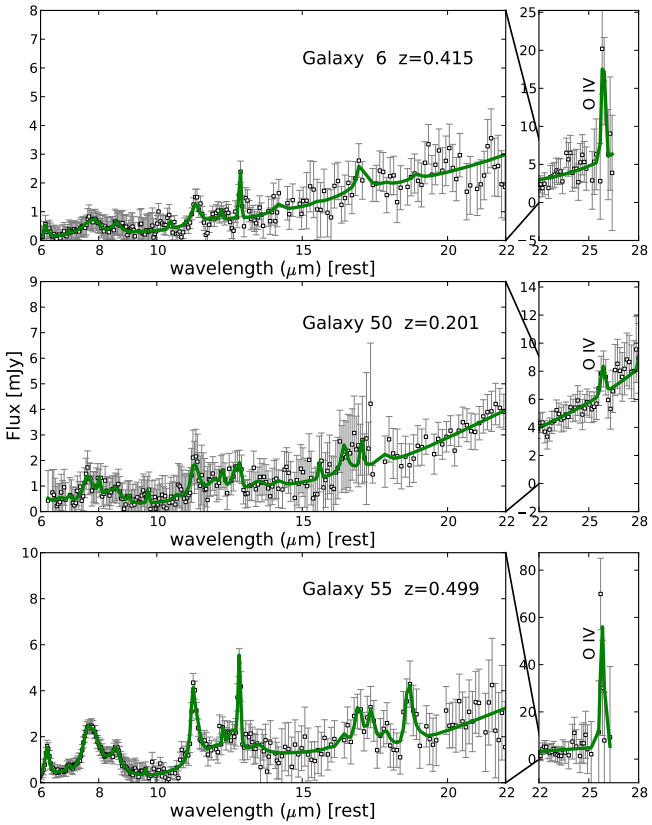

Figure 16. The IRS mid-IR spectra of three non-IRAGN galaxies in our IRS sample with excess [O IV] emission and no other indications of an AGN. The continuous spectrum of each galaxy is shown, but split to better show the spectrum and excess [O IV] emission. Note range of y-axis differs from left to right panel for each spectrum. The open circles are the measured flux densities from the *Spitzer* IRS data observations with error bars representing the uncertainties in those measurements and the green line represents the best fit from spectral decomposition of PAHFIT. All three galaxies show clear emission from [O IV] at 25.9μm.

6.4. *Galaxies with Excess [O IV] λ25.9μm Emission*

Eight galaxies in our IRS sample show unusually high [O IV] emission relative to their PAH luminosities (figure 12), including three galaxies classified as non-IRAGNs (IDs 6, 50, and 55). The excess [O IV] indicates the presence of a hard ionizing field, mostly likely from an AGN that is otherwise undetected in the IR. Here we discuss these "[O IV]-excess" objects in detail.

Figure 16 shows the IRS spectra of all three galaxies (IDs 6, 50, and 55). Both galaxies IDs 6 and 50 have spectra similar to the IRAGN composite spectrum (figure 5) and the spectra of the other IRAGN (figure 4), in our sample. In contrast, galaxy ID 55 has an IRS spectrum more characteristic of the other non-IRAGN (see figures 4 and 5).

We looked for other indications of obscured AGN in the optical spectroscopy (see figure 17) of galaxy IDs 6 and 50, both of which have optical spectra from AGES (galaxy ID 55 lies in the FLS and has optical spectra from Papovich et al. 2006, but the spectral coverage does not extend to Hα and [N II]). We show the portion of the optical spectrum covering the emission lines of [O III] λ5007Å, Hβ λ4861Å, [N II] λ6583Å, and Hα λ6563Å. The optical spectra of all three galaxies (IDs 6, 50, and 55) are typical of star-forming galax-

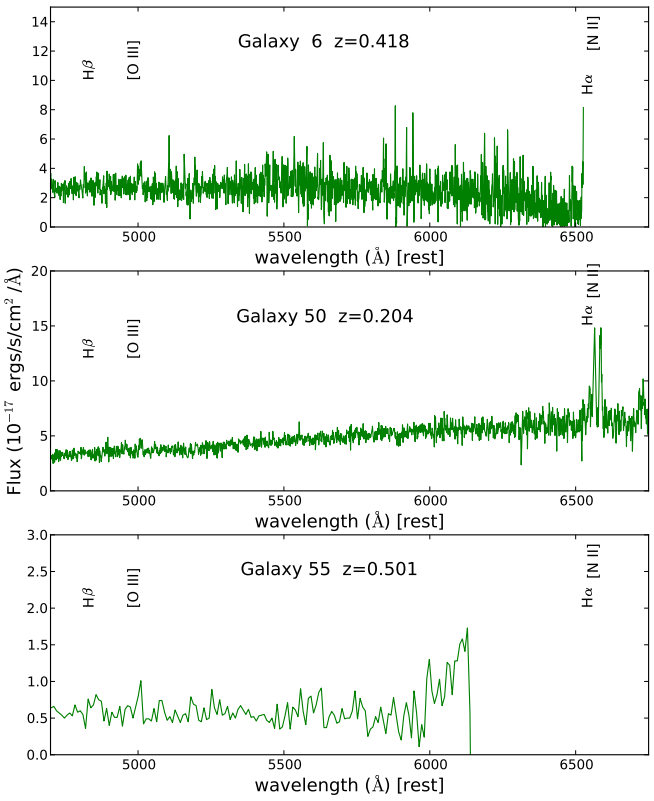

Figure 17. The optical spectra of three non-IRAGN galaxies in our IRS sample with excess [O IV] emission and no other indications of an AGN. Galaxy IDs 6 and 50 are optical spectra from AGES. Galaxy 55 is from the FLS and has an optical spectrum from Papovich et al. (2006). The emission lines of [O III] λ5007Å, Hβ λ4861Å, [N II] λ6583Å, and Hα λ6563Å have been marked to indicate the atomic lines used for optical classification of galaxies as star-forming, composite, or AGN (Kewley et al. 2001; Kauffmann et al. 2003). The redshifts listed for each galaxy are the given optical redshifts from AGES (see table 2).

ies, and therefore the AGN in these galaxies must be very obscured. Using an optical BPT classification (Kewley et al. 2001; Kauffmann et al. 2003) of the galaxies, the galaxies would likely be classified as either star-forming or composite sources. Galaxy ID 50 has all four emission lines used for optical classification and is the most likely source showing any indication of an AGN being present in its optical spectrum.

Of the three non-IRAGN with unusually high [O IV] emission (figure 12, bottom panel), galaxy IDs 6 and 50 both have low L_{PAH}/L_{LIR} ratios, and are quite similar to the values observed in the IRAGN. Galaxy ID 55 has one of the highest L_{PAH}/L_{LIR} ratios in the entire IRS sample. As expected, galaxy IDs 6 and 50 both have low [Ne II] luminosities similar to the five IRAGN with high [O IV] emission (and most of the IRAGN, shown in figure 12). Further evidence for galaxy IDs 6 and 50 being obscured AGN may be seen in that they have optical colors and magnitudes located in the "green valley", similar to the other IRAGN. Furthermore, galaxy No. 55 is about the same as the median value of the non-IRAGN subsample's [Ne II] luminosity (refer to table 3 for fitted flux values). Therefore, galaxy ID 55 is clearly a candidate for an IR-luminous galaxy with a deeply obscured AGN that is otherwise undetected. Further studies of these galaxies would allow for tests of galaxies with deeply obscured AGN, including multi-wavelength observations.

7. CONCLUSIONS

We have studied a sample of 65 galaxies with spectroscopic redshifts of $0.02 < z < 0.6$ using *Spitzer* IRS mid-IR spectroscopy, combined with *Spitzer* imaging and ground-based observations that have flux densities of $f_\nu(24\mu m) > 1.2$ mJy. The galaxies have a total IR luminosity from $\sim 10^{10} L_\odot$ to more than $10^{12} L_\odot$, with a median of $3.0\times10^{11} L_\odot$, which we estimate using the observed MIPS 24 μm data (and 70 and 160 μm when available) combined with Rieke et al. (2009) IR SED templates.

We use an IRAC color–color selection (Stern et al. 2005) to identify IRAGN and non-IRAGN for galaxies in our sample. Our sample includes a wide range of IR-luminous galaxies at redshifts where such galaxies dominate the cosmic IR-luminosity density and SFR-density and they therefore provide insight into the physical processes within these galaxies.

We have shown the measured PAH emission can contribute 11% (75th percentile) or more of the total IR luminosity and half that or slightly more can come from the 7.7μm feature alone, for either the non-IRAGN or IRAGN. The detection frequency of PAH emission (for all features) in the non-IRAGN sample is uniformly more than twice that for IRAGN, except for the 11.3μm feature which is detected only about 1.5 times more frequently in non-IRAGN.

We do not see a significant difference between IRAGN galaxies and non-IRAGN galaxies for short-to-long PAH ratios (namely the 7.7μm-to-11.3μm ratio versus the [Ne III]/[Ne II] ratio) in contrast to other studies (Smith et al. 2007; O'Dowd et al. 2009; Wu et al. 2010). However, the sample galaxies used by these other studies include more nearby galaxies, where the IRS slit encompasses only the nuclear emission. In our sample, the IRS slit contains more of the integrated emission from the galaxy. The data used by these other studies are therefore more sensitive to the destruction of smaller grains from AGN-driven shocks that lower the emission of shorter wavelength PAH features (6.2μm and 7.7μm features, Diamond-Stanic & Rieke 2010). We investigated this by using the H_2 S(3) rotational line (at 9.67μm) and found that none of our galaxies had strong H_2 emission. In fact, we did not have many detections of H_2 emission (only 10 of 65 galaxies have H_2 flux detections at $\geq 3\sigma$) for our sample. This result suggests that if shocks are present in the members of our sample they are not strong enough to dramatically alter the observed short-to-long PAH ratios.

The PAH emission correlates very tightly with the [Ne II] emission. We conclude that both processes correlate with the total SFR, implying that we can use the PAH emission to estimate the contribution of star-formation to the total IR luminosity in the IRAGN. As expected for the IRAGN, the dominant source of IR luminosity comes from the AGN. In fact, we find only about 10%–50% of the contribution comes from star-formation for most of the IRAGN in our sample. The IRAGN have lower [Ne II] emission indicating that the presence of an AGN does not require strong star-formation, and/or that the presence of an AGN suppresses star-formation. The

PAH emission does not correlate as well with [O IV] emission, which is more sensitive to the ionization radiation from the AGN. At a basic level, this shows that AGN do not increase PAH emission. We do identify a population of galaxies with low PAH emission and excess [O IV] emission, indicative of heavily-obscured AGN. Of the eight galaxies with excess [O IV] emission, three are non-IRAGN, with no other indications of AGN from their IRAC colors or optical spectroscopy. Nonetheless, two of these three have suppressed PAH features indicating they have obscured AGN; the third shows no such effects, and its AGN may be very strongly obscured.

Investigating the color-magnitude relation, the IRAGN span the full range of $(u-r)_{0.1}$ colors as do the non-IRAGN for the full sample of IR-luminous galaxies. The optical colors of the IRAGN are more consistent with the distribution of other AGN samples, mostly populating the top of the star-forming blue sequence to the red sequence (see, e.g., Nandra et al. 2007; Weiner et al. 2007). Because no significant difference is seen between IRAGN and non-IRAGN, it is unclear if the presence of an AGN is driving redder $(u-r)_{0.1}$ colors in the IRAGN of IR luminous galaxies. Moreover, most of the IRAGN have lower star-formation (because they show weak [Ne II] emission). Therefore, star-formation is not a necessary component for an AGN to persist.

We thank the anonymous referee for valuable comments that improved the quality of this work. We thank our colleagues on the NDWFS, AGES teams. We thank JD Smith for comments that helped improve the manuscript. This work made use of images and/or data products provided by the NOAO Deep Wide-Field Survey (Jannuzi & Dey 1999; Jannuzi et al. 2004; Dey et al. 2004), which is supported by the National Optical Astronomy Observatory (NOAO). NOAO is operated by AURA, Inc., under a cooperative agreement with the National Science Foundation. Support for this work was provided to the authors by the George P. and Cynthia Woods Mitchell Institute for Fundamental Physics and Astronomy. The research of AD is supported by NOAO, which is operated by the Association of Universities for Research in Astronomy, Inc., under a cooperative agreement with the NSF. This work is based in part on observations and archival data obtained with the Spitzer Space Telescope, which is operated by the Jet Propulsion Laboratory, California Institute of Technology under a contract with NASA. Partial support for this work was provided by NASA through awards 1255094 and 1365085 issued by JPL/Caltech.

REFERENCES

Allamandola, L. J., Tielens, A. G. G. M., & Barker, J. R. 1985, ApJ, 290, L25
—. 1989, ApJS, 71, 733
Armus, L., Charmandaris, V., Bernard-Salas, J., et al. 2007, ApJ, 656, 148
Ashby, M. L. N., Stern, D., Brodwin, M., et al. 2009, ApJ, 701, 428
Bell, E. F., Papovich, C., Wolf, C., et al. 2005, ApJ, 625, 23
Bell, E. F., Wolf, C., Meisenheimer, K., et al. 2004, ApJ, 608, 752
Blanton, M. R., Hogg, D. W., Bahcall, N. A., et al. 2003, ApJ, 594, 186
Brandl, B. R., Bernard-Salas, J., Spoon, H. W. W., et al. 2006, ApJ, 653, 1129
Bundy, K., Georgakakis, A., Nandra, K., et al. 2008, ApJ, 681, 931
Chary, R. & Elbaz, D. 2001, ApJ, 556, 562
Chen, Y., Lowenthal, J. D., & Yun, M. S. 2010, ApJ, 712, 1385
Dale, D. A. & Helou, G. 2002, ApJ, 576, 159
Dey, A., Jannuzi, B. T., Brown, M. J. I., et al. 2004, in Bulletin of the American Astronomical Society, Vol. 36, American Astronomical Society Meeting Abstracts #204, 746
Diamond-Stanic, A. M. & Rieke, G. H. 2010, ApJ, 724, 140
Diamond-Stanic, A. M., Rieke, G. H., & Rigby, J. R. 2009, ApJ, 698, 623
Donley, J. L., Koekemoer, A. M., Brusa, M., et al. 2012, ApJ, 748, 142
Donley, J. L., Rieke, G. H., Pérez-González, P. G., et al. 2008, ApJ, 687, 111
Draine, B. T. & Li, A. 2001, ApJ, 551, 807
Faber, S. M., Willmer, C. N. A., Wolf, C., et al. 2007, ApJ, 665, 265
Frayer, D. T., Fadda, D., Yan, L., et al. 2006, AJ, 131, 250
Genzel, R., Lutz, D., Sturm, E., et al. 1998, ApJ, 498, 579
Gordon, K. D., Engelbracht, C. W., Rieke, G. H., et al. 2008, ApJ, 682, 336
Ho, L. C. & Keto, E. 2007, ApJ, 658, 314
Houck, J. R., Soifer, B. T., Weedman, D., et al. 2005, ApJ, 622, L105
Jannuzi, B. T. & Dey, A. 1999, in Astronomical Society of the Pacific Conference Series, Vol. 191, Photometric Redshifts and the Detection of High Redshift Galaxies, ed. R. Weymann, L. Storrie-Lombardi, M. Sawicki, & R. Brunner, 111
Jannuzi, B. T., Dey, A., Brown, M. J. I., et al. 2004, in Bulletin of the American Astronomical Society, Vol. 36, American Astronomical Society Meeting Abstracts, 1478
Kauffmann, G., Heckman, T. M., Tremonti, C., et al. 2003, MNRAS, 346, 1055
Kewley, L. J., Dopita, M. A., Sutherland, R. S., et al. 2001, ApJ, 556, 121
Kochanek, C. S., Eisenstein, D. J., Cool, R. J., et al. 2012, ApJS, 200, 8
Lacy, M., Wilson, G., Masci, F., et al. 2005, ApJS, 161, 41
Le Floc'h, E., Papovich, C., Dole, H., et al. 2005, ApJ, 632, 169
Leger, A. & Puget, J. L. 1984, A&A, 137, L5
Meléndez, M., Kraemer, S. B., Armentrout, B. K., et al. 2008, ApJ, 682, 94
Mendez, A. J., Coil, A. L., Aird, J., et al. 2013, ArXiv e-prints
Nandra, K., Georgakakis, A., Willmer, C. N. A., et al. 2007, ApJ, 660, L11
O'Dowd, M. J., Schiminovich, D., Johnson, B. D., et al. 2009, ApJ, 705, 885
Oke, J. B. & Gunn, J. E. 1983, ApJ, 266, 713
Papovich, C. & Bell, E. F. 2002, ApJ, 579, L1
Papovich, C., Cool, R., Eisenstein, D., et al. 2006, AJ, 132, 231
Rieke, G. H., Alonso-Herrero, A., Weiner, B. J., et al. 2009, ApJ, 692, 556
Rigby, J. R., Diamond-Stanic, A. M., & Aniano, G. 2009, ApJ, 700, 1878
Roussel, H., Helou, G., Hollenbach, D. J., et al. 2007, ApJ, 669, 959
Rujopakarn, W., Rieke, G. H., Weiner, B. J., et al. 2013, ApJ, accepted
Schawinski, K., Thomas, D., Sarzi, M., et al. 2007, MNRAS, 382, 1415
Schawinski, K., Urry, C. M., Virani, S., et al. 2010, ApJ, 711, 284
Schutte, W. A., Tielens, A. G. G. M., & Allamandola, L. J. 1993, ApJ, 415, 397
Schweitzer, M., Lutz, D., Sturm, E., et al. 2006, ApJ, 649, 79
Shang, Z., Brotherton, M. S., Wills, B. J., et al. 2011, ApJS, 196, 2
Smith, J. D. T., Draine, B. T., Dale, D. A., et al. 2007, ApJ, 656, 770
Stern, D., Eisenhardt, P., Gorjian, V., et al. 2005, ApJ, 631, 163
Tielens, A. G. G. M. 2005, The Physics and Chemistry of the Interstellar Medium, ed. Tielens, A. G. G. M.
Weiner, B. J., Papovich, C., Bundy, K., et al. 2007, ApJ, 660, L39
Wu, Y., Helou, G., Armus, L., et al. 2010, ApJ, 723, 895
Wyder, T. K., Martin, D. C., Schiminovich, D., et al. 2007, ApJS, 173, 293

Table 2
Galaxy Classifications and Locations

ID	AOR	R.A.	Dec.	z(opt)	z(IRS)	f(24μm) [mJy]	f(70μm) [mJy]	f(160μm) [mJy]	$L(IR)_R$ [$10^{10}L_\odot$]	AGN
1	14127872	14h25m00.18s	+32d59m50.0s	0.296	0.304	4.97 ± 0.02	60.7 ± 1.09	...	31.9	
2	21757184	14h25m27.91s	+33d47m47.0s	0.509	0.516	5.38 ± 0.02	17.4 ± 1.38	...	94.6	Y
3	14129920	14h25m44.96s	+33d37m05.0s	0.321	0.344	3.01 ± 0.01	...	...	24.8	Y
4	14087680	14h25m52.68s	+34d02m40.1s	0.562	0.565	11.36 ± 0.02	258.2 ± 1.03	413.0 ± 1.12	268.	Y
5	14133248	14h26m07.93s	+34d50m45.0s	0.405	0.407	2.77 ± 0.01	47.5 ± 1.09	143.9 ± 1.21	39.0	
6	14133504	14h26m18.65s	+34d57m03.0s	0.418	0.415	1.58 ± 0.01	...	...	35.8	
7	14084352	14h26m23.88s	+32d44m35.8s	0.171	0.173	12.17 ± 0.02	304.1 ± 1.03	474.2 ± 1.04	31.1	Y
8	14126080	14h26m59.13s	+33d33m05.0s	0.150	0.150	16.12 ± 0.19	178.6 ± 1.25	...	22.9	
9	21758464	14h27m44.37s	+34d29m08.2s	0.365	0.365	1.56 ± 0.01	109.4 ± 1.06	234.4 ± 1.12	59.1	
10	21758208	14h27m50.32s	+35d04m51.2s	0.211	0.210	4.82 ± 0.01	87.1 ± 1.07	206.1 ± 1.15	17.2	
11	14132480	14h28m19.51s	+33d51m50.0s	0.488	0.490	1.70 ± 0.01	22.3 ± 1.24	101.9 ± 1.24	53.4	
12	14132992	14h28m19.57s	+34d23m34.0s	0.474	0.493	2.05 ± 0.01	18.9 ± 1.22	...	54.0	Y
13	14086144	14h28m49.79s	+34d32m40.2s	0.216	0.218	8.09 ± 0.03	253.5 ± 1.04	598.4 ± 1.06	47.5	
14	14132736	14h29m19.77s	+34d15m06.0s	0.424	0.425	1.64 ± 0.01	23.3 ± 1.16	92.7 ± 1.26	37.9	
15	14132224	14h29m35.97s	+33d37m13.0s	0.419	0.422	1.90 ± 0.01	33.3 ± 1.17	131.8 ± 1.20	38.8	
16	21758720	14h29m50.66s	+35d08m42.7s	0.366	0.380	5.87 ± 0.01	19.2 ± 1.25	...	53.8	Y
17	21755648	14h29m51.38s	+32d50m36.0s	0.270	0.268	3.39 ± 0.01	19.1 ± 1.22	...	16.8	Y
18	14129408	14h30m00.39s	+35d38m14.0s	0.240	0.240	9.11 ± 0.02	125.3 ± 1.06	146.9 ± 1.15	28.0	
19	21756672	14h30m19.82s	+33d40m47.2s	0.231	0.233	2.62 ± 0.01	44.9 ± 1.15	97.3 ± 1.21	11.4	
20	14082304	14h30m24.46s	+32d56m16.4s	0.042	0.042	36.68 ± 0.15	483.1 ± 1.04	824.1 ± 1.08	4.56	
21	14086400	14h31m14.77s	+33d46m23.0s	0.230	0.231	4.53 ± 0.03	153.5 ± 1.09	347.5 ± 1.07	31.1	
22	14081792	14h31m19.76s	+35d34m18.0s	0.034	0.036	33.58 ± 0.11	537.0 ± 1.03	691.8 ± 1.06	3.11	
23	14082048	14h31m21.12s	+35d37m21.8s	0.035	0.036	33.18 ± 0.46	1318.3 ± 1.04	2779.7 ± 1.04	11.4	
24	14130432	14h31m21.88s	+34d40m46.0s	0.348	0.354	3.19 ± 0.01	17.1 ± 1.20	...	27.4	Y
25	14080768	14h31m25.43s	+33d13m49.7s	0.022	0.022	33.98 ± 0.54	794.3 ± 1.06	1011.6 ± 1.07	2.04	
26	21756160	14h31m33.98s	+33d45m16.0s	0.490	0.494	2.46 ± 0.01	22.8 ± 1.22	...	54.4	Y
27	14081536	14h31m56.23s	+33d38m33.1s	0.034	0.035	29.27 ± 0.50	...	...	1.67	
28	14083840	14h32m28.36s	+34d58m38.8s	0.129	0.130	3.15 ± 0.02	137.1 ± 1.13	258.8 ± 1.22	7.63	
29	14086912	14h32m34.90s	+33d28m32.3s	0.249	0.253	3.85 ± 0.02	338.8 ± 1.03	395.4 ± 1.09	46.6	
30	14086656	14h32m39.56s	+35d01m51.3s	0.236	0.237	10.73 ± 0.02	236.6 ± 1.03	349.9 ± 1.07	42.9	
31	14131968	14h32m52.49s	+33d11m53.0s	0.401	0.395	2.58 ± 0.01	28.2 ± 1.21	...	32.4	
32	14128128	14h33m26.18s	+33d05m58.0s	0.243	0.245	4.28 ± 0.02	62.1 ± 1.08	119.4 ± 1.21	16.6	
33	21755904	14h33m33.34s	+33d09m22.0s	0.353	0.356	2.37 ± 0.01	...	...	24.9	Y
34	21757440	14h33m42.17s	+34d56m51.0s	0.494	0.494	2.24 ± 0.01	...	...	54.4	
35	14083584	14h34m45.32s	+33d13m46.1s	0.073	0.075	14.46 ± 0.03	288.4 ± 1.03	485.3 ± 1.08	7.01	
36	14130176	14h34m53.85s	+34d27m44.0s	0.329	0.324	3.56 ± 0.01	29.4 ± 1.15	...	25.5	
37	21756416	14h35m00.65s	+33d29m23.0s	0.274	0.285	2.61 ± 0.01	70.0 ± 1.08	140.6 ± 1.16	20.1	
38	14081024	14h35m18.21s	+35d07m08.3s	...	0.029	169.23 ± 3.72	3926.4 ± 1.04	5571.9 ± 1.04	19.7	
39	14130688	14h35m19.42s	+35d36m22.0s	0.316	0.318	2.92 ± 0.01	26.5 ± 1.24	...	20.8	Y
40	21758976	14h35m35.47s	+33d25m44.4s	0.244	0.251	6.07 ± 0.02	104.2 ± 1.06	145.5 ± 1.18	24.9	
41	14134272	14h36m06.84s	+35d09m27.0s	0.525	0.525	1.22 ± 0.01	21.0 ± 1.22	...	63.1	
42	14125824	14h36m19.14s	+33d29m17.0s	0.188	0.190	7.07 ± 0.05	...	...	17.8	
43	14087168	14h36m28.12s	+33d33m58.0s	0.265	0.269	10.82 ± 0.03	223.4 ± 1.04	267.3 ± 1.11	51.0	
44	14128640	14h36m33.16s	+33d48m05.0s	0.218	0.245	6.43 ± 0.02	12.4 ± 1.38	...	25.4	Y
45	14129152	14h36m36.65s	+34d50m34.0s	0.279	0.274	4.05 ± 0.02	39.2 ± 1.12	...	21.0	
46	14081280	14h36m41.23s	+34d58m24.2s	0.030	0.030	16.75 ± 0.25	...	...	0.84	
47	14130944	14h37m11.26s	+35d40m36.0s	0.362	0.362	3.42 ± 0.02	223.9 ± 1.04	236.0 ± 1.16	64.0	
48	21757952	14h37m23.73s	+35d07m35.0s	0.579	0.551	4.78 ± 0.01	30.5 ± 1.15	...	96.2	
49	21757696	14h37m52.92s	+35d32m51.4s	0.563	0.565	2.36 ± 0.01	68.7 ± 1.10	217.3 ± 1.10	101.	
50	21756928	14h38m09.88s	+35d27m37.8s	0.204	0.201	2.70 ± 0.02	31.7 ± 1.15	...	8.74	
51	14127104	17h12m39.64s	+58d41m48.0s	0.165	0.166	10.06 ± 0.13	...	...	18.3	
52	14131712	17h13m08.57s	+60d16m21.0s	0.332	0.333	4.65 ± 0.09	76.2 ± 12.20	...	36.7	
53	14135552	17h14m27.02s	+58d38m36.0s	0.562	0.565	1.30 ± 0.06	...	...	75.6	
54	14127360	17h14m37.44s	+59d56m48.1s	0.196	0.198	12.38 ± 0.14	...	...	30.8	
55	14135808	17h15m25.74s	+60d04m24.0s	0.501	0.499	1.34 ± 0.06	...	...	55.8	
56	14127616	17h15m42.00s	+59d16m57.4s	0.116	0.118	26.78 ± 0.21	...	...	19.7	
57	14126336	17h19m16.60s	+59d34m49.0s	0.166	0.170	17.06 ± 0.17	177.5 ± 27.00	...	30.2	
58	14131200	17h20m25.19s	+59d15m03.0s	0.305	0.307	3.28 ± 0.08	...	...	21.3	
59	14134528	17h20m46.74s	+59d22m23.0s	0.539	0.526	1.26 ± 0.06	...	...	63.4	
60	14134784	17h21m17.75s	+58d51m20.0s	0.512	0.493	1.54 ± 0.06	...	...	54.1	Y
61	14135040	17h21m18.31s	+58d46m01.0s	0.555	0.559	1.22 ± 0.05	...	...	73.5	Y
62	14126592	17h22m20.27s	+59d09m49.0s	0.179	0.179	9.66 ± 0.13	180.4 ± 27.50	...	21.3	
63	14131456	17h23m48.13s	+59d01m54.0s	0.321	0.324	4.26 ± 0.09	...	...	29.9	
64	14126848	17h24m00.61s	+59d02m28.0s	0.178	0.180	12.82 ± 0.14	...	...	26.5	
65	14135296	17h25m03.37s	+59d11m09.0s	0.514	0.515	1.30 ± 0.06	...	...	60.2	

Note. — Optical redshifts [z(opt)] are from the AGES catalog (Kochanek et al. 2012) and Papovich et al. (2006) for FLS sources. IRS redshifts [z(IRS)] are from the fits as discussed in section 4.3. The 24μm flux densities are from the AGES catalog (Kochanek et al. 2012) and Papovich et al. (2006) for FLS sources and discussed in sections 3.1 and 3.2. The 70μm and 160μm flux densities are from MAGES (B. Jannuzi et al., in prep) and discussed in sections 3.1 and 3.2. L_{IR} values are described in section 5.2 and appendix A and the selection of IRAGN in section 3.3.

Table 3
Fitted Fluxes of the Most Prominent PAH Emission Features

ID	$F_{6.2}$ $[10^{-17}]$	$F_{7.7}$ $[10^{-16}]$	$F_{8.6}$ $[10^{-17}]$	$F_{11.3}$ $[10^{-17}]$	$F_{12.7}$ $[10^{-17}]$	$F_{17.0}$ $[10^{-17}]$
1	4.50 ± 1.45	2.48 ± 0.41	19.3 ± 2.30	0.39 ± 0.54	6.42 ± 0.56	...
2	0.30 ± 1.47	0.67 ± 0.72	0.79 ± 2.67	1.07 ± 0.75	1.48 ± 1.14	1.73 ± 0.54
3	...	0.26 ± 0.22	1.09 ± 0.75	0.39 ± 0.15	0.23 ± 0.33	0.99 ± 1.55
4	7. 4 ± 0.69	3.31 ± 0.34	12.2 ± 1.46	6.97 ± 1.74	6.65 ± 2.62	2.57 ± 0.85
5	6.37 ± 0.60	2.12 ± 0.24	6.92 ± 0.98	6.49 ± 0.77	3.49 ± 0.68	3.19 ± 2.28
6	0.58 ± 0.48	0.30 ± 0.17	0.78 ± 0.41	1.02 ± 0.19	0.12 ± 0.29	0.74 ± 0.90
7	7.5 ± 1.62	5.58 ± 0.48	14.6 ± 1.57	13.5 ± 1.49	7.30 ± 2.49	5.12 ± 3.88
8	17.2 ± 0.94	6.45 ± 0.33	8.0 ± 1.03	16.6 ± 0.90	9.28 ± 1.48	8.38 ± 1.56
9	11.4 ± 1.52	3.46 ± 0.67	12.4 ± 2.39	9.90 ± 1.85	6.50 ± 1.16	2.11 ± 0.66
10	7.48 ± 5.79	2.34 ± 0.79	7.76 ± 2.03	7.95 ± 2.16	7.84 ± 2.58	6.69 ± 3.23
11	7.01 ± 0.68	2.34 ± 0.23	7.49 ± 1.23	6.61 ± 0.82	4.50 ± 0.51	2.14 ± 1.79
12	0.88 ± 0.54	0.56 ± 0.23	1.27 ± 0.78	0.70 ± 0.40	0.46 ± 0.17	0.11 ± 0.27
13	26.7 ± 1.01	9.80 ± 0.51	29.2 ± 1.68	23.8 ± 1.75	14.8 ± 1.53	8.19 ± 3.29
14	4.45 ± 0.68	1.31 ± 0.27	4.98 ± 1.37	7.59 ± 1.20	1.63 ± 0.87	2.62 ± 2.14
15	5.12 ± 0.70	1.75 ± 0.28	5.69 ± 1.09	4.95 ± 0.77	3.76 ± 0.71	2.26 ± 1.94
16	1.42 ± 1.69	0.16 ± 0.74	0.95 ± 2.01	2.15 ± 1.67	1.80 ± 1.72	1.28 ± 0.85
17	2.07 ± 3.19	0.59 ± 0.54	2.28 ± 2.02	2.10 ± 1.13	1.14 ± 1.42	1.73 ± 2.26
18	9.08 ± 0.91	2.60 ± 0.34	10.1 ± 1.05	8.75 ± 0.85	3.96 ± 0.71	6.74 ± 1.14
19	1.76 ± 1.61	0.76 ± 0.43	2.23 ± 1.31	2.44 ± 1.12	1.55 ± 1.14	0.91 ± 0.60
20	28.6 ± 0.77	9.29 ± 0.37	28.8 ± 1.08	26.3 ± 0.86	16.1 ± 0.91	18.1 ± 1.51
21	10.8 ± 0.69	3.88 ± 0.33	21.4 ± 1.22	10.9 ± 1.24	5.57 ± 1.18	2.99 ± 2.42
22	43.1 ± 0.87	15.7 ± 0.36	223.1 ± 1.08	42.6 ± 0.76	24.9 ± 1.14	30.0 ± 1.75
23	81.0 ± 1.51	30.9 ± 0.49	79.6 ± 1.82	231.3 ± 1.39	38.4 ± 1.32	58.1 ± 2.25
24	1.18 ± 0.71	0.60 ± 0.28	2.40 ± 0.98	1.39 ± 0.40	0.47 ± 0.16	0.74 ± 1.87
25	22.1 ± 0.90	7.34 ± 0.40	21.8 ± 0.87	21.8 ± 0.64	9.89 ± 0.89	256.8 ±25.17
26	3.43 ± 1.00	1.22 ± 0.31	3.85 ± 1.00	3.43 ± 0.66	2.65 ± 1.16	1.96 ± 1.50
27	27.2 ± 0.88	10.7 ± 0.35	37.7 ± 1.10	30.1 ± 0.86	16.1 ± 1.06	270.9 ± 1.76
28	7.17 ± 0.67	2.65 ± 0.22	7.75 ± 0.66	7.86 ± 0.60	5.62 ± 0.59	5.78 ± 1.02
29	5.88 ± 0.51	2.60 ± 0.19	8.07 ± 0.64	6.09 ± 0.69	2.15 ± 0.39	3.41 ± 1.03
30	11.9 ± 0.76	4.33 ± 0.41	16.1 ± 1.25	14.4 ± 1.24	8.55 ± 0.98	5.06 ± 2.62
31	1.81 ± 0.66	0.54 ± 0.12	1.84 ± 0.78	3.01 ± 0.49	0.83 ± 0.55	3.19 ± 1.54
32	5.40 ± 0.91	1.47 ± 0.40	5.83 ± 1.08	6.79 ± 0.80	2.90 ± 0.60	2.60 ± 0.95
33	0.89 ± 0.52	0.32 ± 0.08	1.23 ± 0.66	0.82 ± 0.52	0.76 ± 0.84	1.11 ± 0.66
34	0.55 ± 0.47	0.31 ± 0.18	1.50 ± 0.85	0.45 ± 0.67	0.84 ± 1.20	0.25 ± 0.27
35	10.6 ± 1.06	3.84 ± 0.40	12.2 ± 1.22	13.7 ± 1.00	7.25 ± 1.01	12.7 ± 2.08
36	1.61 ± 1.13	0.63 ± 0.17	1.88 ± 0.82	2.08 ± 0.52	1.49 ± 0.51	0.37 ± 0.53
37	1.96 ± 0.68	1.07 ± 0.16	2.83 ± 0.67	3.24 ± 0.88	2.85 ± 0.84	0.27 ± 0.33
38	61.5 ± 0.89	385.5 ± 0.43	66.5 ± 1.22	77.2 ± 1.04	39.6 ± 1.18	173. ± 4.74
39	1.67 ± 1.03	0.79 ± 0.29	2.71 ± 1.16	1.74 ± 0.64	1.28 ± 0.37	2.01 ± 2.61
40	7.97 ± 3.22	2.41 ± 0.71	7.85 ± 2.82	6.70 ± 2.50	5.25 ± 2.36	5.57 ± 8.23
41	1.67 ± 0.42	0.60 ± 0.19	2.06 ± 0.88	3.71 ± 0.43	2.56 ± 0.73	2.24 ± 1.75
42	7.96 ± 1.22	2.37 ± 0.27	7.35 ± 1.15	4.79 ± 1.12	9.65 ± 0.37	7.60 ± 1.54
43	10.1 ± 0.96	4.13 ± 0.35	10.7 ± 1.14	7.72 ± 1.43	5.83 ± 1.64	4.68 ± 2.36
44	0.80 ± 0.84	0.68 ± 0.34	0.55 ± 0.83	2.19 ± 0.39	0.24 ± 0.13	0.01 ± 0.42
45	2.81 ± 1.01	0.90 ± 0.34	3.45 ± 0.97	3.30 ± 0.49	0.44 ± 0.50	0.91 ± 0.67
46	17.4 ± 0.79	6.54 ± 0.40	20.8 ± 1.01	20.3 ± 0.93	10.0 ± 0.83	21.9 ± 1.85
47	3.97 ± 1.37	1.66 ± 0.54	7.86 ± 2.36	6.19 ± 2.01	1.31 ± 0.90	1.94 ± 2.02
48	0.47 ± 0.73	0.05 ± 0.14	0.60 ± 1.57	...	0.40 ± 0.96	1.09 ± 1.18
49	4.19 ± 0.39	1.83 ± 0.18	4.64 ± 0.74	4.81 ± 1.10	3.28 ± 1.40	1.51 ± 1.32
50	0.37 ± 7.50	0.37 ± 0.20	1.90 ± 1.51	2.01 ± 1.56	0.78 ± 1.17	0.91 ± 1.36
51	18.2 ± 1.36	6.27 ± 0.33	21.5 ± 1.00	19.3 ± 0.98	12.2 ± 0.58	6.54 ± 0.75
52	9.22 ± 0.80	2.83 ± 0.29	10.0 ± 1.26	9.88 ± 0.61	4.36 ± 0.63	5.59 ± 0.79
53	2.66 ± 1.12	0.97 ± 0.40	2.92 ± 1.56	3.62 ± 1.78	1.46 ± 1.49	1.33 ± 0.89
54	5.86 ± 0.88	2.16 ± 0.28	5.94 ± 0.79	6.65 ± 0.77	5.25 ± 1.13	1.19 ± 0.49
55	3.73 ± 0.56	1.08 ± 0.24	3.54 ± 1.00	5.52 ± 0.97	2.01 ± 0.55	2.86 ± 2.47
56	44.3 ± 5.43	8.94 ± 1.77	28.6 ± 5.48	29.0 ± 5.00	20.8 ± 3.42	16.9 ± 4.31
57	16.0 ± 4.62	4.44 ± 0.71	11.3 ± 2.86	8.66 ± 3.22	5.01 ± 1.34	1.37 ± 0.61
58	6.92 ± 0.60	2.20 ± 0.26	7.06 ± 0.87	8.03 ± 0.77	4.40 ± 0.49	3.69 ± 2.28
59	0.65 ± 0.57	0.24 ± 0.22	1.43 ± 0.99	0.32 ± 0.34	0.31 ± 0.34	1.48 ± 0.83
60	1.04 ± 0.51	0.35 ± 0.09	1.42 ± 0.49	1.04 ± 0.22	0.83 ± 0.72	2.13 ± 0.88
61	1.50 ± 0.43	0.60 ± 0.20	2.67 ± 0.79	1.11 ± 0.27	0.09 ± 0.47	0.41 ± 0.54
62	9.76 ± 1.21	3.45 ± 0.31	11.3 ± 0.95	13.0 ± 0.92	6.90 ± 0.49	4.58 ± 0.67
63	4.87 ± 0.66	1.67 ± 0.18	5.24 ± 0.62	4.39 ± 0.39	3.20 ± 0.49	1.85 ± 0.82
64	9.25 ± 1.76	3.14 ± 0.40	8.46 ± 1.31	11.5 ± 1.26	4.78 ± 1.26	4.92 ± 2.03
65	3.85 ± 0.56	1.14 ± 0.20	3.90 ± 1.09	3.05 ± 0.63	0.44 ± 0.16	2.16 ± 1.65

Note. — Integrated fluxes in W/m^2 from PAHFIT spectral decomposition for the PAH Emission features. Values given as (...) do not have a measured flux from PAHFIT spectral decomposition.

Table 4
Fitted Fluxes of the Most Prominent Atomic Emission Lines

ID	$F_{[NeII]}$ $[10^{-18}]$	$F_{[NeIII]}$ $[10^{-18}]$	$F_{[OIV]}$ $[10^{-18}]$	$F_{[H_2S(3)]}$ $[10^{-18}]$
1	8.84 ± 1.25	10.6 ± 1.30	1.52 ± 4.16	24.5 ± 20.9
2	...	...	1.75 ± 0.49	3.15 ± 3.68
3	2.25 ± 0.70	...	...	0.52 ± 1.23
4	15.0 ± 3.55	3.56 ± 4.51	2.17 ± 0.59	9.78 ± 5.04
5	11.2 ± 1.04	1.33 ± 3.02	...	1.62 ± 1.57
6	3.03 ± 0.76	0.17 ± 2.81	14.9 ± 5.49	0.02 ± 1.19
7	26.0 ± 2.75	4.24 ± 2.33	7.54 ± 2.23	46.1 ± 9.36
8	22.6 ± 2.07	12.0 ± 1.68	...	0.48 ± 1.17
9	14.5 ± 2.96	1.52 ± 3.35	1.70 ± 5.54	5.09 ± 4.81
10	14.0 ± 3.53	3.33 ± 4.20	...	3.40 ± 4.24
11	7.65 ± 1.24	...	1.25 ± 0.36	2.81 ± 1.66
12	...	...	0.81 ± 0.23	0.39 ± 0.70
13	25.2 ± 2.18	2.69 ± 2.36	5.97 ± 3.18	6.04 ± 3.00
14	6.46 ± 1.00	3.23 ± 3.01	...	6.61 ± 5.54
15	5.74 ± 1.01	...	...	0.93 ± 1.85
16	2.49 ± 3.30	2.75 ± 5.95	23.2 ± 7.35	1.70 ± 3.21
17	3.37 ± 1.76	2.85 ± 2.14	...	0.77 ± 4.28
18	17.7 ± 0.86	6.50 ± 0.91	2.24 ± 2.44	7.11 ± 2.98
19	1.05 ± 1.08	0.87 ± 1.64	...	0.32 ± 2.08
20	51.3 ± 1.41	9.63 ± 1.94	2.30 ± 1.48	3.77 ± 1.19
21	16.3 ± 1.70	1.15 ± 4.65	1.04 ± 1.71	2.10 ± 2.06
22	226.8 ± 1.73	11.5 ± 1.63	4.82 ± 16.5	8.08 ± 1.29
23	235.8 ± 1.95	13.1 ± 1.68	11.6 ± 1.45	13.4 ± 3.34
24	1.33 ± 0.67	8.98 ± 1.50	6.43 ± 4.13	1.19 ± 1.76
25	25.8 ±25.25	42.9 ±25.34	...	25.99 ±25.25
26	3.13 ± 1.46	0.89 ± 1.18	20.8 ± 0.67	0.62 ± 1.27
27	35.3 ± 1.67	8.80 ± 1.45	2.19 ± 1.61	7.71 ± 1.56
28	28.11 ± 0.96	0.91 ± 0.77	2.60 ± 0.69	1.66 ± 1.51
29	9.12 ± 0.97	0.99 ± 0.91	1.04 ± 1.29	9.11 ± 2.84
30	27.4 ± 2.43	7.72 ± 2.65	...	17.1 ± 3.86
31	2.65 ± 0.75	1.17 ± 2.78	...	3.83 ± 5.45
32	9.22 ± 0.90	2.27 ± 0.70	...	1.13 ± 1.74
33	1.99 ± 1.14	9.76 ± 40.0	3.06 ± 2.65	0.40 ± 1.32
34	0.58 ± 1.55	0.52 ± 1.40	0.52 ± 0.15	1.76 ± 1.98
35	16.7 ± 1.36	2.78 ± 1.51	1.68 ± 1.88	3.60 ± 2.64
36	3.35 ± 0.60	0.26 ± 0.87	1.91 ± 2.85	0.49 ± 3.05
37	...	1.66 ± 1.51	0.51 ± 1.63	...
38	86.2 ± 1.69	60.7 ± 3.56	12.4 ± 5.60	10.5 ± 1.40
39	1.99 ± 0.75	1.36 ± 1.01	2.52 ± 7.10	4.18 ± 4.63
40	6.87 ± 3.45	2.37 ± 3.43	3.17 ± 3.98	2.99 ± 6.70
41	6.07 ± 1.26	3.24 ± 1.87	0.50 ± 0.14	3.08 ± 0.99
42	42.4 ± 1.18	5.81 ± 0.94	...	3.48 ± 2.45
43	24.3 ± 2.38	4.42 ± 2.69	...	4.72 ± 2.74
44	0.65 ± 0.62	2.44 ± 0.74	...	1.02 ± 1.92
45	6.30 ± 0.70	...	2.90 ± 1.13	0.23 ± 1.42
46	20.1 ± 1.16	4.73 ± 1.29	1.28 ±46.27	46.71 ± 1.32
47	7.03 ± 1.30	2.10 ± 2.71	2.43 ± 5.68	14.0 ± 20.8
48	0.46 ± 4.35	0.51 ± 4.18	0.69 ± 0.19	13.3 ± 22.0
49	6.70 ± 1.90	2.56 ± 1.31	1.06 ± 0.29	1.95 ± 1.57
50	2.18 ± 1.50	0.96 ± 1.58	2.98 ± 1.86	2.49 ± 3.60
51	51.1 ± 0.80	7.58 ± 0.68	1.76 ± 1.31	4.08 ± 1.29
52	11.8 ± 0.98	6.27 ± 1.02	5.50 ± 1.14	5.18 ± 3.71
53	1.53 ± 1.79	6.88 ± 3.58	0.68 ± 0.19	1.29 ± 2.55
54	12.4 ± 1.51	11.6 ± 1.71	4.18 ± 1.33	1.11 ± 1.26
55	8.55 ± 1.32	...	64.4 ± 18.3	1.82 ± 2.39
56	36.9 ± 3.98	9.21 ± 2.81	...	10.2 ± 11.4
57	9.29 ± 1.65	6.66 ± 1.44	...	17.3 ± 12.4
58	13.0 ± 0.87	4.23 ± 1.06	3.16 ± 2.89	0.94 ± 1.17
59	...	0.36 ± 1.39	0.43 ± 0.12	1.18 ± 0.78
60	0.93 ± 0.62	0.61 ± 1.42	22.4 ± 5.32	0.42 ± 0.71
61	0.56 ± 0.55	...	0.56 ± 0.15	0.19 ± 0.36
62	13.9 ± 0.61	2.05 ± 0.45	5.89 ± 1.07	3.40 ± 1.48
63	7.29 ± 0.65	1.84 ± 0.48	1.80 ± 1.05	1.16 ± 0.98
64	19.9 ± 1.60	2.96 ± 1.38	...	6.93 ± 3.25
65	7.76 ± 0.93	...	0.61 ± 0.17	3.18 ± 2.48

Note. — Integrated fluxes in W/m^2 from PAHFIT spectral decomposition for the atomic emission lines. Values given as (...) do not have a measured flux from PAHFIT spectral decomposition.

Table 5
Equivalent Widths for Various PAH Emission Features

ID	$EW_{6.2}$	$EW_{7.7}$	$EW_{8.6}$	$EW_{11.3}$
1	1.96 ± 0.22	4.46 ± 0.20	3.99 ± 0.11	0.07 ± 0.01
2	0.02 ± 0.03	0.41 ± 0.12	0.05 ± 0.04	0.09 ± 0.02
3	0.02 ± 0.07	0.60 ± 0.22	0.27 ± 0.05	0.10 ± 0.01
4	0.36 ± 0.03	1.76 ± 0.11	0.76 ± 0.05	0.52 ± 0.04
5	2.57 ± 1.67	7.03 ± 1.88	2.39 ± 0.36	2.54 ± 0.14
6	0.56 ± 2.56	2.58 ± 1.51	0.64 ± 0.51	0.64 ± 0.09
7	0.33 ± 0.02	2.23 ± 0.12	0.91 ± 0.05	1.42 ± 0.09
8	1.81 ± 0.11	5.99 ± 0.30	1.65 ± 0.06	1.54 ± 0.03
9	2.39 ± 1.30	6.09 ± 1.72	2.33 ± 0.46	2.34 ± 0.25
10	1.25 ± 0.48	3.63 ± 0.98	1.43 ± 0.30	2.23 ± 0.29
11	5.98 ± 0.65	9.76 ± 0.90	2.62 ± 0.20	2.11 ± 0.11
12	0.14 ± 0.03	1.09 ± 0.10	0.26 ± 0.04	0.17 ± 0.02
13	1.72 ± 0.14	6.84 ± 0.66	2.55 ± 0.17	2.93 ± 0.08
14	1.69 ± 0.73	4.08 ± 0.95	1.96 ± 0.36	4.03 ± 0.40
15	2.19 ± 4.17	6.45 ± 3.07	2.21 ± 0.50	2.37 ± 0.17
16	0.10 ± 0.05	0.47 ± 0.10	0.07 ± 0.04	0.20 ± 0.03
17	2.12 ± 1.68	2.63 ± 0.98	0.84 ± 0.31	0.53 ± 0.10
18	0.71 ± 0.06	1.72 ± 0.10	0.82 ± 0.04	0.98 ± 0.03
19	0.91 ± 64.86	4.04 ± 60.40	1.38 ± 5.30	1.68 ± 0.62
20	1.90 ± 0.20	5.43 ± 0.28	1.71 ± 0.04	1.75 ± 0.12
21	1.42 ± 0.23	5.73 ± 0.99	2.23 ± 0.29	2.67 ± 0.30
22	3.28 ± 0.16	10.27 ± 0.23	3.01 ± 0.04	1.91 ± 0.02
23	2.75 ± 0.07	10.80 ± 0.24	3.14 ± 0.05	2.55 ± 0.02
24	0.08 ± 0.03	0.68 ± 0.09	0.35 ± 0.04	0.30 ± 0.02
25	2.10 ± 0.27	6.26 ± 0.37	25.87 ± 0.06	25.86 ± 0.03
26	0.65 ± 0.15	2.60 ± 0.27	0.85 ± 0.07	0.84 ± 0.04
27	1.91 ± 0.11	7.41 ± 0.24	2.40 ± 0.05	1.51 ± 0.03
28	0.93 ± 0.06	3.64 ± 0.31	1.41 ± 0.08	2.35 ± 0.10
29	1.23 ± 0.09	5.30 ± 0.36	2.02 ± 0.13	1.92 ± 0.12
30	0.61 ± 0.03	2.51 ± 0.15	1.20 ± 0.06	1.86 ± 0.06
31	0.35 ± 0.66	1.04 ± 0.90	0.51 ± 0.27	1.33 ± 0.14
32	0.81 ± 0.36	2.10 ± 0.51	0.97 ± 0.12	1.76 ± 0.09
33	0.13 ± 0.03	0.58 ± 0.08	0.24 ± 0.04	0.20 ± 0.02
34	0.32 ± 1.20	2.68 ± 1.06	1.29 ± 0.30	0.21 ± 0.06
35	0.90 ± 0.07	3.18 ± 0.24	1.20 ± 0.07	1.74 ± 0.05
36	0.35 ± 0.36	1.41 ± 0.61	0.48 ± 0.17	0.77 ± 0.10
37	2.50 ± 0.63	6.61 ± 1.26	1.59 ± 0.31	1.69 ± 0.24
38	1.89 ± 0.06	7.01 ± 0.16	1.88 ± 0.03	38.14 ± 0.01
39	0.35 ± 2.53	2.00 ± 1.93	0.95 ± 0.54	0.84 ± 0.13
40	6.17 ± 7.58	8.36 ± 4.45	2.21 ± 0.88	1.33 ± 0.23
41	0.72 ± 0.32	2.68 ± 0.56	1.01 ± 0.18	3.20 ± 0.25
42	2.93 ± 0.61	7.50 ± 0.97	2.29 ± 0.22	1.12 ± 0.14
43	1.17 ± 0.11	4.05 ± 0.30	1.13 ± 0.06	0.86 ± 0.05
44	0.07 ± 0.06	0.64 ± 0.30	0.05 ± 0.13	0.25 ± 0.02
45	0.61 ± 0.26	1.84 ± 0.39	0.71 ± 0.10	0.88 ± 0.05
46	2.04 ± 0.33	7.26 ± 0.67	2.32 ± 0.13	1.97 ± 0.14
47	1.73 ± 10.84	5.96 ± 6.75	4.64 ± 2.36	4.56 ± 0.69
48	0.25 ± 1.00	0.19 ± 0.47	0.21 ± 0.26	0.01 ± 0.06
49	2.39 ± 2.13	13.13 ± 2.43	3.25 ± 0.43	2.06 ± 0.22
50	0.19 ± 10.89	1.74 ± 27.35	0.97 ± 4.52	1.30 ± 0.45
51	2.71 ± 0.51	7.61 ± 0.39	2.52 ± 0.09	2.30 ± 0.04
52	0.91 ± 0.08	2.76 ± 0.38	1.27 ± 0.11	2.18 ± 0.17
53	1.00 ± 0.37	2.97 ± 0.58	0.90 ± 0.15	1.20 ± 0.10
54	1.26 ± 0.10	4.08 ± 0.25	1.09 ± 0.06	1.09 ± 0.04
55	2.35 ± 2.39	4.32 ± 1.61	1.50 ± 0.33	2.54 ± 0.26
56	2.04 ± 0.49	4.47 ± 0.68	1.85 ± 0.21	2.35 ± 0.14
57	1.65 ± 0.35	3.91 ± 0.52	1.57 ± 0.57	0.98 ± 0.10
58	4.12 ± 1.17	8.85 ± 1.27	2.64 ± 0.27	2.97 ± 0.15
59	0.20 ± 0.16	0.85 ± 0.18	0.54 ± 0.09	0.15 ± 0.03
60	0.21 ± 0.09	0.71 ± 0.15	0.33 ± 0.06	0.39 ± 0.03
61	0.37 ± 0.06	1.92 ± 0.15	0.95 ± 0.07	0.49 ± 0.03
62	1.09 ± 0.12	4.02 ± 0.42	1.47 ± 0.10	2.26 ± 0.06
63	3.76 ± 3.92	11.72 ± 2.02	2.92 ± 0.28	1.22 ± 0.04
64	0.89 ± 0.11	2.79 ± 0.25	0.92 ± 0.06	1.41 ± 0.04
65	4.75 ± 1.04	6.75 ± 1.18	2.09 ± 0.29	1.53 ± 0.10

Note. — Equivalent widths are from PAHFIT spectral decomposition results and the errors were done using monte carlo simulations and running through PAHFIT to get uncertainties. Values given as (...) do not have a measured flux from PAHFIT spectral decomposition.

APPENDIX

ESTIMATING THE TOTAL IR LUMINOSITY

At the redshifts of our sample, $0.02 < z < 0.6$, the MIPS IR data probe the rest-frame mid-to-far-IR, which broadly correlates with the total IR luminosity (e.g. Chary & Elbaz 2001; Papovich & Bell 2002; Rieke et al. 2009). We used models (Chary & Elbaz 2001; Dale & Helou 2002; Rieke et al. 2009) for the IR SED of galaxies to convert the observed MIPS data to total IR luminosity. By selection, all galaxies in our sample have 24μm detections, and we convert the observed 24μm flux densities to rest-frame luminosity densities at 24μm/$(1+z)$. We then correct these values to a total IR luminosity, $L_{IR}(24\mu m)$, using *each* of the three sets of model IR SEDs, assuming for each set of models that a given rest-frame 24μm/$(1+z)$ luminosity density translates uniquely to a single SED template. The Rieke et al. (2009) templates apply to local galaxies and do not include the SED evolution seen at high redshift. However, Rujopakarn et al. (2013) show that the local SEDs and those appropriate for high redshift converge for the redshift range of our sample.

For those galaxies with detections at 70μm and/or 160μm in the MAGES data (as listed in table 2), we use all available MIPS flux densities to estimate the total IR luminosity. For each source, we convert the observed MIPS data to rest-frame luminosity densities, and scaled each IR SED in each set of models with a multiplicative factor to obtain a best-fit for each SED. For each set of models, we minimized a χ^2 statistic with $\chi^2_a = \sum(d_i - c \times m_i^a)^2/\sigma_i$, where d_i is the rest-frame luminosity density measured from the i=24μm, 70μm, and 160μm data, $m_{(a,i)}$ is the luminosity density expected for model IR SED a, c is the fitted scale factor, and σ_i are the errors on the measured MIPS data. We chose the IR SED from each set of models that minimizes χ^2_a.

In figure 18, we compare the $L_{IR}(24\mu m)$ against the L_{IR} derived using multiple MIPS bands (24μm, 70μm and/or 160μm) for each of the three sets of IR SED models (Chary & Elbaz 2001; Dale & Helou 2002; Rieke et al. 2009). We found that there is no more than a factor of 2-3 difference in the derived IR luminosity from multiple MIPS bands and that derived from 24μm only between any of the IR SED models. This is particularly true for galaxies with total IR luminosities $L_{IR} > 10^{11} L_\odot$ (the majority of L_{IR} estimates in our sample). However, our far-IR (160μm sources) sample is incomplete in the direction that the less luminous galaxies ($L_{IR} < 10^{11} L_\odot$) will be under-represented. As illustrated in figure 18 and discussed below, the IR luminosities derived from the 24μm data only from the Rieke et al. (2009) SED templates are the most consistent with the IR luminosities derived using multiple MIPS bands. In particular, for IRAGN the IR luminosities derived with the Rieke et al. (2009) SED templates with only 24μm data are consistent with those from multiple MIPS bands. We find the median ratio estimates of the total IR luminosity (using all bands available) compared to the total IR luminosity (using only the 24μm band) for the Chary & Elbaz (2001), Dale & Helou (2002), and Rieke et al. (2009) models to be 0.97, 0.96, and 1.0, respectively.

We considered the idea that the IR SED templates we used for the IRAGN may be incorrect, which could be the case for those IRAGN with only 24μm detections. Specifically, we computed the total IR luminosities from the 24 micron flux densities for the IRAGN using the SEDs for optically luminous quasars (Shang et al. 2011). In these cases the total IR luminosities for the IRAGN would decrease by at most a factor of five (at most a factor of 3.5 for the IRAGN with only 24μm detections). Because there are only four IRAGN with only 24μm detections, and the effect is not large ($\approx$0.5 dex in L_{IR}), this would not change any of our conclusions if all of these IRAGN have SEDs of optical luminous quasars. However, the MIPS-to-IRAC colors of the IRAGN in our sample ($F_{24\mu m}/F_{8.0\mu m} = 4.2$ median and ranging from 3.5 to 6.1 for the four IRAGN with only 24μm detections) are highly discrepant compared to those of the Shang et al. (2011) optically luminous SEDs ($F_{24\mu m}/F_{8.0\mu m} = 1.4$ median). Therefore, it seems highly unlikely that the IRAGN in our sample have SEDs like optical QSOs[10]. In this case, we take the lower IR luminosity of a factor of 3.5 to be a lower bound for an extreme case for the IRAGN in our sample.

We found that when only the 24μm and 70μm flux densities are available the estimates of the total IR luminosity are similar to those derived using 24μm only for the Rieke et al. (2009) SED models. And when using the Chary & Elbaz (2001) and Dale & Helou (2002) models the estimates for the total IR luminosity are smaller compared to the that derived with only the 24μm flux density by a median of 0.97 and 0.95, respectively. When all three MIPS flux densities are available the estimate of the total IR luminosity is larger compared to that derived by 24μm only (larger by a median of 1.34, 1.61, and 1.44 for the Rieke et al. (2009), Chary & Elbaz (2001), and Dale & Helou (2002) SED models, respectively). One conclusion from this analysis is that objects in our sample detected at 160μm appear to have a large cold-dust mass which is not sufficiently probed by the 24μm and 70μm bandpasses. However, since the 160μm detections are not complete and preferentially find galaxies with larger-than-typical flux densities, the larger luminosity estimates may have a contribution due to selection bias.

For these reasons, we adopt the IR luminosities derived using the Rieke et al. (2009) SED templates for this work. For all galaxies in our sample, we use the IR luminosity derived from all available MIPS bands.

[10] Indeed, we have an optical spectrum for one of the IRAGN with only 24μm detection and it only shows narrow lines indicative of a Seyfert galaxy, clearly not a broad-line quasar.

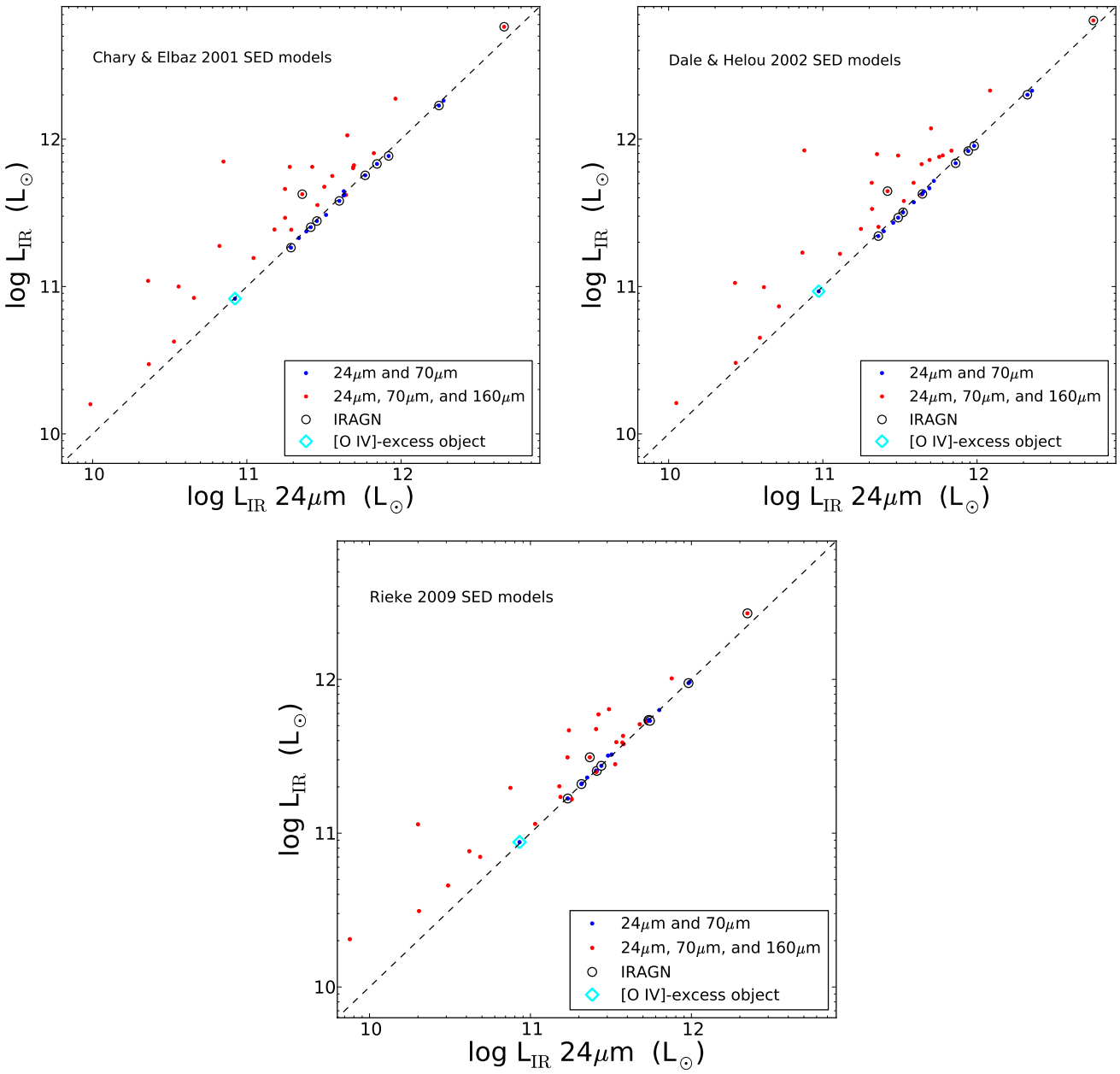

Figure 18. The IR luminosities derived from the 24μm data only $L_{IR}(24\mu m)$ compared to the L_{IR} derived using multiple MIPS bands (24μm, 70μm and/or 160μm) for each of the three sets of IR SED models (Chary & Elbaz 2001; Dale & Helou 2002; Rieke et al. 2009, as labeled in each panel). The dashed line represents a unity relation between the two L_{IR} estimates. Sources with only 24μm flux densities are not plotted.